UCSF

UC San Francisco Previously Published Works

Title

Empirical Bayesian localization of event-related time-frequency neural activity dynamics

Permalink

https://escholarship.org/uc/item/51p72943

Authors

Cai, Chang

Hinkley, Leighton

Gao, Yijing

et al.

Publication Date

2022-09-01

DOI

10.1016/j.neuroimage.2022.119369

Peer reviewed

eScholarship.org Powered by the California Digital Library
University of California

Author Manuscript

Author Manuscript

Author Manuscript

Author Manuscript

HHS Public Access

Author manuscript

Neuroimage. Author manuscript; available in PMC 2023 August 09.

Published in final edited form as:

Neuroimage. 2022 September ; 258: 119369. doi:10.1016/j.neuroimage.2022.119369.

Empirical Bayesian localization of event-related time-frequency neural activity dynamics

Chang Cai[a,b,*], **Leighton Hinkley**[b], **Yijing Gao**[b], **Ali Hashemi**[c,d,e], **Stefan Haufe**[c,f], **Kensuke Sekihara**[g,h], **Srikantan S. Nagarajan**[b,**]

[a]National Engineering Research Center for E-Learning, Central China Normal University, Wuhan, China

[b]Department of Radiology and Biomedical Imaging, University of California, San Francisco, CA 94143-0628, United States

[c]Berlin Center for Advanced Neuroimaging, Charité Universitätsmedizin Berlin, Berlin, Germany

[d]Machine Learning Group, Electrical Engineering and Computer Science Faculty, Technische Universität Berlin, Germany

[e]Institut für Mathematik, Technische Universität Berlin, Germany

[f]Bernstein Center for Computational Neuroscience Berlin, Berlin, Germany

[g]Department of Advanced Technology in Medicine, Tokyo Medical and Dental University, 1-5-45 Yushima, Bunkyo-ku, Tokyo 113–8519, Japan

[h]Signal Analysis Inc., Hachioji, Tokyo, Japan

Abstract

Accurate reconstruction of the spatio-temporal dynamics of event-related cortical oscillations across human brain regions is an important problem in functional brain imaging and human cognitive neuroscience with magnetoencephalography (MEG) and electroencephalography (EEG). The problem is challenging not only in terms of localization of complex source configurations from sensor measurements with unknown noise and interference but also for reconstruction of transient event-related time-frequency dynamics of cortical oscillations. We recently proposed a robust empirical Bayesian algorithm for simultaneous reconstruction of complex brain source activity and noise covariance, in the context of evoked and resting-state data. In this paper, we expand upon this empirical Bayesian framework for optimal reconstruction of event-related time-

This is an open access article under the CC BY-NC-ND license (http://creativecommons.org/licenses/by-nc-nd/4.0/)

[*]Corresponding author at: National Engineering Research Center for E-Learning, Central China Normal University, Wuhan, China. ccai@ccnu.edu.cn (C. Cai). [**]Corresponding author at: Department of Radiology and Biomedical Imaging, University of California, San Francisco, CA 94143-0628, United States. sri@ucsf.edu (S.S. Nagarajan).

Credit authorship contribution statement

Chang Cai: Conceptualization, Methodology, Software, Validation, Formal analysis, Investigation, Data curation, Writing – original draft, Writing – review & editing, Visualization, Funding acquisition. **Leighton Hinkley:** Methodology, Data curation, Writing – review & editing. **Yijing Gao:** Conceptualization. **Ali Hashemi:** Writing – review & editing. **Stefan Haufe:** Conceptualization, Methodology, Writing – review & editing. **Kensuke Sekihara:** Conceptualization, Methodology, Validation, Formal analysis, Investigation, Writing – original draft, Writing – review & editing. **Srikantan S. Nagarajan:** Conceptualization, Methodology, Validation, Formal analysis, Investigation, Data curation, Writing – original draft, Writing – review & editing, Visualization, Supervision, Project administration, Funding acquisition.

Author Manuscript Author Manuscript Author Manuscript Author Manuscript

frequency dynamics of regional cortical oscillations, referred to as time-frequency Champagne (TFC). This framework enables imaging of five-dimensional (space, time, and frequency) event-related brain activity from M/EEG data, and can be viewed as a time-frequency optimized adaptive Bayesian beamformer. We evaluate TFC in both simulations and several real datasets, with comparisons to benchmark standards-variants of time-frequency optimized adaptive beamformers (TFBF) as well as the sLORETA algorithm. In simulations, we demonstrate several advantages in estimating time-frequency cortical oscillatory dynamics compared to benchmarks. With real MEG data, we demonstrate across many datasets that the proposed approach is robust to highly correlated brain activity and low SNR data, and is able to accurately reconstruct cortical dynamics with data from just a few epochs.

Keywords

Dynamics of neural activity; Brain source power changes; Five-dimensional neuroimaging; Electromagnetic brain imaging; Bayesian inference

1. Introduction

Noninvasive functional brain imaging has made a tremendous impact in improving our understanding of the human brain. Functional magnetic resonance imaging (fMRI) has been the predominant modality for imaging the functioning brain since the middle of 1990s, as it can produce images with high spatial resolution. However, due to reliance on the blood oxygenation response, fMRI lacks the temporal resolution required to image the dynamic and oscillatory spatiotemporal patterns associated with activities in the brain. In contrast to fMRI, magnetoencephalography (MEG) and electroencephalography (EEG) are other popular non-invasive techniques which measure electromagnetic fields emanating from the brain with excellent temporal resolution. This level of resolution has clinical utility, as high temporal and frequency resolution is essential for epileptic waveform activity localization (Guggisberg et al., 2008; Velmurugan et al., 2019). It has also shown to be essential for cognitive neuroscience imaging studies using M/EEG that examine dynamic brain networks subserving perception, action and cognition (Borghesani et al., 2020; Herman et al., 2013; Hinkley et al., 2011; Ranasinghe et al., 2020).

Since M/EEG sensors are located outside the head, examining sensor data does not provide sufficient information about which brain structures generated the activity of interest. To extract more precise information about underlying brain activities, it is essential to apply electromagnetic brain source localization algorithms which are solutions to the ill-posed biomagnetic inverse problem. Many inverse algorithms have been proposed for solving the bioelectromagnetic inverse problem, i.e., for estimating the parameters of neural source activity from MEG and EEG sensor data, including linear (van Drongelen et al., 1996; Gross et al., 2003; Hämäläinen and Ilmoniemi, 1994; Schmidt, 1986; Stoica and Nehorai, 1990; Van Veen et al., 1997) and non-linear methods (Friston et al., 2008; Gramfort et al., 2013; Wipf et al., 2010a), distributed (Pascual-Marqui, 2002) vs sparse (Gramfort et al., 2013; Wipf et al., 2010a).

Author Manuscript Author Manuscript Author Manuscript Author Manuscript

In functional neuroimaging studies, two distinct types of neural source activity have been examined – phase-locked and non-phase locked event-related brain activity. Phase-locked activity is usually obtained in evoked-response paradigms by averaging activity across repeated events. Many algorithms have been proposed in the literature for examining phase-locked activity (Gramfort et al., 2013; Hämäläinen and Ilmoniemi, 1994; Pascual-Marqui, 2002; Uutela et al., 1999; Wipf et al., 2010a). A key feature contributing to accurate estimation of phase-locked activity is that the power of phase-locked activity following an event is greater than a pre-event baseline period, and this activity is dominated by low frequencies (1–8 Hz). In contrast, non-phase locked activity is reconstructed by extracting signal magnitude (and phase) in single trials. Importantly, such event-related power fluctuations can manifest as either an increase or a decrease in power. Furthermore, power increases and decreases will be frequency-specific. There have been only a few papers that have described algorithms for accurate reconstructions of time-window and frequency specific event-related non-phase locked brain activity (Dalal et al., 2008a; Gross et al., 2001; Limpiti et al., 2008).

In our previous work, we proposed an adaptive optimised time frequency Beamformer (TFBF) which enables accurate reconstruction of five-dimensional event-related non-phase locked brain activity by using segmented filtered data to obtain the weight matrix and is able to estimate the change in power from a control (i.e., baseline) time window to an active time window (Dalal et al., 2008a). However, the method suffers from sensitivity to inaccurate sample data covariance matrices that are used to obtain the weight matrix, especially under high correlated brain sources or limited time series data availability and low signal-to-noise ratio (SNR), for example, in cognitive paradigms. Although modifications to the Beamformer algorithm have been developed to address the issue of correlated source reconstruction, they have met with varying success and are further limited by requiring a-priori information on source location (Dalal et al., 2006), being limited to scalar sources rather than vector sources (Brookes et al., 2006), or by being limited to two sources due to computation time constraints (Diwakar et al., 2010; 2011).

Recently, for phase-locked brain activity, we proposed a family of robust empirical Bayesian algorithms, e.g., Champagne (Cai et al., 2020; Hashemi et al., 2021b; Sekihara and Nagarajan, 2015; Wipf et al., 2010b) and its extensions (Hashemi et al., 2021a; 2021c; Hashemi and Haufe, 2018), which are able to reconstruct complex brain activity and learn the noise covariance simultaneously, and which has been successfully applied in M/EEG source imaging. In this paper, we expand this empirical Bayesian framework for reconstruction of event-related non-phase locked time-frequency dynamics of regional cortical oscillations. We refer to this extension as time-frequency Champagne (TFC). This TFC framework enables imaging of five-dimensional (space, time, and frequency) event-related brain activity from M/EEG data. The key idea here that allows for reconstructions of event-related activity in both task and control periods is the use of sparse Bayesian reconstruction algorithms on omnibus data, which includes both task and control time-windows (Robinson and Vrba, 1999; Singh et al., 2003; Vrba and Robinson, 2001).

Here, we evaluate TFC both in simulations and on several real datasets, with comparisons to benchmark standards-variants of time-frequency optimized adaptive beamformers (TFBF)

Author Manuscript Author Manuscript Author Manuscript Author Manuscript

as well as the sLORETA algorithm. In simulations, we demonstrate several advantages in estimating time-frequency cortical oscillatory dynamics compared to benchmarks. With real MEG data, we demonstrate across many datasets that the proposed approach is robust to highly correlated brain activity and low SNR data, and is able to accurately reconstruct cortical dynamics with data from just a few epochs.

2. Methods

This section first briefly introduces the generative model for neural dynamics and the problem of imaging dynamics of frequency-specific neural activity. Following this, we introduce the time-frequency Champagne algorithm (TFC) algorithm for estimation of neural dynamics. Finally, we show the relationship of TFC to TFBF.

2.1. The generative model

The sensor level data measured on or near the scalp can be modeled as:

$$\boldsymbol{Y} = \boldsymbol{L}\boldsymbol{S} + \boldsymbol{\varepsilon} = \sum_{n=1}^{N} \boldsymbol{L}_n \boldsymbol{S}_n + \boldsymbol{\varepsilon}, \tag{1}$$

where $\boldsymbol{Y} = [\boldsymbol{y}(1), \cdots, \boldsymbol{y}(T)] \in \mathbb{R}^{M \times T}$ is the measured sensor data, M is the number of channels measured, and T is the number of time samples. $\boldsymbol{L} = [\boldsymbol{L}_1, \ldots, \boldsymbol{L}_N] \in \mathbb{R}^{M \times d_c N}$ is the leadfield matrix obtained from the forward model, and $d_c N = d_c \times N$, which we assume to have d_c orientations for each voxel. $\boldsymbol{S} = \left[\boldsymbol{S}_1^\top, \ldots, \boldsymbol{S}_N^\top\right]^\top \in \mathbb{R}^{d_c N \times T}$ is the unknown brain activity. $\boldsymbol{S}_n = \left[\boldsymbol{s}_n^1, \cdots, \boldsymbol{s}_n^{d_c}\right]^\top \in \mathbb{R}^{d_c \times T}$ is the n-th voxel intensity. N denotes the number of voxels under consideration and $\boldsymbol{L}_n = \left[\boldsymbol{l}_n^1, \cdots, \boldsymbol{l}_n^{d_c}\right] \in \mathbb{R}^{M \times d_c}$ denotes the leadfield matrix for the n-th voxel. The i-th column of $\boldsymbol{L}_n$ represents the signal vector that would be observed at the scalp given a unit current source or dipole at the n-th voxel with a fixed orientation in the i-th direction. The voxel dimension d_c is usually set to 3. In event-related data analysis, we always segment the sensor data into control and task periods which are expressed as $\boldsymbol{Y}_C$ and $\boldsymbol{Y}_T$.

2.2. Imaging dynamics of frequency-specific neural activity

In many neuroscience paradigms, it is necessary to compute the dynamics of event-related non-phase locked neural activity for specific experimental or cognitive tasks, which could be obtained by contrasting activity in multiple activation windows, across different frequency bands, or by comparison to activity during one or multiple baseline windows. The resulting contrast spectrograms are time frequency representation of non-phase locked event-related brain source activity.

In previous work, we have proposed an adaptive spatial filtering algorithm optimized for robust source time frequency reconstruction, which maximizes the ultimate potential of M/EEG for five-dimensional imaging of brain activity in space, time, and frequency and renders it applicable for widespread studies of human cortical dynamics during cognition (Dalal et al., 2008b). We directly computed spectrograms of the source time series during a

Author Manuscript Author Manuscript Author Manuscript Author Manuscript

task time-period of interest by contrasting it with the spectrogram of a control time period where the brain sources of interest are expected to not be active.

To quantify this task-induced activity, first, the sensor data $\boldsymbol{Y}$ is passed through a filter bank and then divided into control and task periods, which are denoted as $\boldsymbol{Y}_C(f)$ and $\boldsymbol{Y}_T(f)$ for f-th band. Task periods are then segmented into overlapping task windows, which are expressed as $\boldsymbol{Y}_T(k, f)$ ($k = 1, \cdots, K$, we assume the number of segmented task time windows is K, the lower case k refers to the index of the overlapping task time window). To estimate the change from a control time window to a k-th task time window at n-th voxel, we first estimate the source power from each windows at n-th voxel, denoted as $P_C(n, f)$ and $P_T(n, k, f)$, then the following equation to calculate the F-ratio of power contrast in decibels is expressed as:

$$\boldsymbol{F}(n, k, f) = 10 \log_{10} \frac{P_T(n, k, f)}{P_C(n, f)}, \tag{2}$$

Since MEG and EEG measure signals data outside brain, we need to estimate the underlying brain source activity from sensor data in both task and control time windows using inverse reconstruction algorithms.

Naive use of the above F-ratio to quantify task-induced brain activity in conjunction with sparse reconstruction algorithms can however often lead to divide-by-zero errors for the most interesting voxels of interest, i.e. the voxels which are activated in the task-window but have no activity in the control period resulting a zero in the denominator. Moreover, if there are strong correlated brain sources, then beamformer reconstruction of power in both task- and control-windows will be inaccurate, rendering the F-ratio calculation inaccurate as well. Here, we propose a solution to avoid both of these problems with an adaptation of Champagne, a sparse Bayesian algorithm.

2.3. Time-frequency Champagne algorithm

In our prior work, we introduced the robust empirical Bayesian algorithm Champagne, which is able to reconstruct complex brain activity and estimate the source activation power (Cai et al., 2020). However, instead of estimating the Champagne source reconstruction estimate for power in task and control time-windows separately, and to directly compute the power ratio at each voxel, here we propose a modified approach for Eq. (2). Since Champagne is a sparse reconstruction algorithm, naive estimation of the denominator, i.e. source power in control period, will result in zero activity for many voxels and consequently result in divide-by-zero errors for the calculation of the F-ratio in Eq. (2).

To circumvent this problem and to improve the robustness of the F-ratio calculation, we estimate the power in task and control periods and propose using a spatial weight matrix derived from the omnibus data that includes both task and control time-windows $\boldsymbol{Y}_O(k, f) = [\boldsymbol{Y}_C(f), \boldsymbol{Y}_T(k, f)]$. We then estimate omnibus hyperparameters $\boldsymbol{\alpha}_O$ and the well-regularized omnibus data covariance $\boldsymbol{\Sigma}_O(k, f)$, and use these inferred parameters to estimate the source power in task and control windows. The idea of using omnibus data has been used in conjunction with adaptive beamforming for MEG by others (Robinson and Vrba,

Author Manuscript Author Manuscript Author Manuscript Author Manuscript

1999; Singh et al., 2003; Vrba and Robinson, 2001) and ensures robustness and avoids the divide-by-zero errors.

This modified time-frequency Champagne algorithm with noise learning (Cai et al., 2021) is shown in Appendix A. Specifically, we obtain the brain source power from k-th task window and the control window at n-th voxel in f-th frequency band $\widehat{P}_T(n,k,f)$ and $\widehat{P}_C(n,k,f)$,

$$\widehat{P}_T(n,k,f) = \alpha_O^2(n,k,f)\mathrm{tr}\left(\boldsymbol{L}_n^\top \boldsymbol{\Sigma}_O^{-1}(k,f)\boldsymbol{\Sigma}_T(k,f)\boldsymbol{\Sigma}_O^{-1}(k,f)\boldsymbol{L}_n\right), \tag{3}$$

$$\widehat{P}_C(n,k,f) = \alpha_O^2(n,k,f)\mathrm{tr}\left(\boldsymbol{L}_n^\top \boldsymbol{\Sigma}_O^{-1}(k,f)\boldsymbol{\Sigma}_C(f)\boldsymbol{\Sigma}_O^{-1}(k,f)\boldsymbol{L}_n\right), \tag{4}$$

where, $\alpha_O(n,k,f)$ is the prior variance of the n-th voxel for the omnibus data, $\boldsymbol{\Sigma}_T(k,f)$, $\boldsymbol{\Sigma}_C(f)$, and $\boldsymbol{\Sigma}_O(k,f)$ are well-regularized model covariances for the task, control and omnibus data respectively which are robust to limited numbers of data samples. Consequently, when $\alpha_O(n,k,f)$ is not equal to zero, this F-ratio as described above corresponds to voxels that are active in either the task or the control periods, which is expressed as:

$$\boldsymbol{F}^{TFC}(n,k,f) = 10\log_{10}\frac{\mathrm{tr}\left(\boldsymbol{L}_n^\top \boldsymbol{\Sigma}_O^{-1}(k,f)\boldsymbol{\Sigma}_T(k,f)\boldsymbol{\Sigma}_O^{-1}(k,f)\boldsymbol{L}_n\right)}{\mathrm{tr}\left(\boldsymbol{L}_n^\top \boldsymbol{\Sigma}_O^{-1}(k,f)\boldsymbol{\Sigma}_C(f)\boldsymbol{\Sigma}_O^{-1}(k,f)\boldsymbol{L}_n\right)}, \tag{5}$$

In contrast, while $\alpha_O(n,k,f)$ equals to zero, there is no activity in either period, then the F-ratio can be expressed as:

$$\boldsymbol{F}^{TFC}(n,k,f) = 0. \tag{6}$$

The specific steps of the time-frequency Champagne algorithm (TFC) are detailed in Table 1.

In summary, to estimate the five-dimensional dynamics of neural activity, TFC first filters the input sensor data into different frequency bands; then the filtered active sensor data is segmented into overlapping active windows. Subsequently, TFC estimates the model data covariances of control, active and concatenated data using the Champagne algorithm, and finally calculates the neural dynamics using Eq. (5).

2.4. Relationship of TFC to TFBF

Previously, we have proposed a TFBF algorithm to estimate brain sources and their neural dynamics as (Dalal et al., 2008b):

$$\boldsymbol{F}^{TFBF}(n,k,f) = 10\log_{10}\frac{\mathrm{tr}\left(\boldsymbol{W}^\top(n,k,f)\boldsymbol{R}_T(k,f)\boldsymbol{W}(n,k,f)\right)}{\mathrm{tr}\left(\boldsymbol{W}^\top(n,k,f)\boldsymbol{R}_C(f)\boldsymbol{W}(n,k,f)\right)}, \tag{7}$$

where, $\widehat{P}_T^{BF}(n,k,f)$ and $\widehat{P}_C^{BF}(n,k,f)$ are the brain source power from k-th task window and the control window at n-th voxel in f-th frequency band using Beamformer algorithm, $\boldsymbol{R}_T(k,f) \in \mathbb{R}^{M\times M}$ and $\boldsymbol{R}_C(f) \in \mathbb{R}^{M\times M}$ are sample task and control covariances computed

Author Manuscript Author Manuscript Author Manuscript Author Manuscript

for each resulting time-frequency window. $\boldsymbol{W}(n,k,f) \in \mathbb{R}^{M \times d_c}$ is the weight matrix obtained with the omnibus sample data covariance, which is defined as $\boldsymbol{R}_O(k,f)$.

$$\boldsymbol{W}(n,k,f) = \boldsymbol{R}_O^{-1}(k,f)\boldsymbol{L}_n\left(\boldsymbol{L}_n^{\top}\boldsymbol{R}_O^{-1}(k,f)\boldsymbol{L}_n\right)^{-1}. \tag{8}$$

In the TFBF model above, the output power change for each voxel is determined by the lead field matrix $\boldsymbol{L}_n$, the omnibus data covariance $\boldsymbol{R}_O(k,f)$, and the sample data covariances from task $\boldsymbol{R}_T(k,f)$ and control windows $\boldsymbol{R}_C(f)$.

The fidelity of power change estimation is dramatically affected by the accuracy of the sample data covariance, as well as a variety of other factors such as SNR, source correlations, and the number of time samples T. Since the TFBF algorithm requires that the covariance matrices be invertible, without regularization or with incorrect regularization for covariance matrix inversion, algorithm performance can degrade. Furthermore, if sources are highly correlated, the performance of the estimate can be significantly compromised, a well-known problem for adaptive beamformers. Finally, if the number of sample time points T is small, then the sample data covariance may deviate sharply from the true covariance, leading to systematic estimation errors. This is partly because when T is small, then even sources produced by an uncorrelated generative model may appear correlated. Consequently, if a more robust version of the sample data covariance were obtained, it would greatly improve the power change estimation. The TFC algorithm we propose here contains a robust way to estimate the power of our brain activity from control and task time window. Theoretically, TFC can be shown to be a particular instantiation of a Bayesian model-based TFBF, which are adaptive beamformers that use model covariances instead of the sample covariance of the data (Al-Shoukairi and Rao, 2019; Pote and Rao, 2020). In the limit of infinite data, the model covariance matrix estimated by TFC will equal the sample covariance, i.e. $\boldsymbol{R} = \boldsymbol{L}\boldsymbol{\alpha}\boldsymbol{L}^{\top} + \boldsymbol{\Lambda} = \boldsymbol{\Sigma}_y$. Therefore, we could replace $\boldsymbol{R}_O(k,f)$, $\boldsymbol{R}_T(k,f)$ and $\boldsymbol{R}_C(f)$ with the corresponding model covariance matrices $\boldsymbol{\Sigma}_O(k,f)$, $\boldsymbol{\Sigma}_T(k,f)$, and $\boldsymbol{\Sigma}_C(k,f)$ respectively in Eqs (7) and (8). Consequently, the F-ratio of power contrast for TFBF can be expressed as:

$$\begin{aligned}\boldsymbol{F}^{TFBF}(n,k,f) &= \frac{\mathrm{tr}\left(\boldsymbol{L}_n^{\top}\boldsymbol{\Sigma}_O^{-1}(k,f)\boldsymbol{\Sigma}_T(k,f)\boldsymbol{\Sigma}_O^{-1}(k,f)\boldsymbol{L}_n\right)}{\mathrm{tr}\left(\boldsymbol{L}_n^{\top}\boldsymbol{\Sigma}_O^{-1}(k,f)\boldsymbol{\Sigma}_C(f)\boldsymbol{\Sigma}_O^{-1}(k,f)\boldsymbol{L}_n\right)} \\ &= \boldsymbol{F}^{TFC}(n,k,f).\end{aligned} \tag{9}$$

Therefore, TFC can be viewed as a particular instantiation of a Bayesian model beamformer that uses model covariance derived from sparse Bayesian learning instead of the sample data covariance.

3. Performance evaluation of simulated and real data

3.1. Benchmark algorithms

We chose to test the TFC algorithm against four representative source localization algorithms from the literature: three adaptive spatial filtering methods, namely time frequency optimized beamformer (TFBF) (Sekihara et al., 2001), Bayesian PCA based

Author Manuscript Author Manuscript Author Manuscript Author Manuscript

TFBF (bPCA_TFBF) (Engemann and Gramfort, 2015; Woolrich et al., 2011), and Variational Bayesian Factor Analysis based TFBF (VBFA_TFBF) (Engemann and Gramfort, 2015; Nagarajan et al., 2007), more details are provided in Appendix B. In addition, one non-adaptive spatial filtering method, sLORETA (Pascual-Marqui, 2002), is included. For sLORETA, we use the default setting defined in the NUTMEG software where the regularization parameter of sLORETA is set as 1e-3 of the maximum eigenvalue of the Gram matrix (Dalal et al., 2004).

3.2. Simulations configurations

Dipolar sources with variable orientation were used to generate the simulated data. Damped sinusoidal time courses were created as point source time activity and then projected to the sensors using the leadfield matrix generated by the forward model. The brain volume was segmented into 8 mm voxels and a three-orientation forward lead field was calculated using a single spherical-shell model Hallez et al. (2007) implemented in NUTMEG (Hinkley et al., 2020a). The parcellation at this resolution yields around 5000 voxels. To evaluate the robustness of the proposed algorithm to noise, we randomly chose segments of real brain noise from actual resting-state sensor recordings of ten human subjects. These recordings are presumed to contain only spontaneous brain activity and sensor noise. SNR and correlations between voxel time courses were varied to examine algorithm performance. SNR and time course correlation are defined in a standard fashion (Cai et al., 2018; Owen et al., 2012).

We first examined the accuracy of TFC with simulations. Fifty trials were generated, spanning-750 ms to 1000 ms per trial with a sampling rate of 1200 Hz and an SNR of 0 dB. Three point sources with sine waves time courses at frequencies of 8 Hz, 21 Hz and 42 Hz were synthesized and placed randomly in the brain source space. We also randomized the phase of each source and varied them between trials. The brain sources time series were windowed such that they represented event-related synchronization (ERS) activity and were not active simultaneously. The first source was active from 50 ms to 300 ms, while the second one was active from 350 ms to 550 ms, and the last source had a baseline activity from −750 ms to 0 ms, then went to zero activity from 0 ms to 600 ms, following which it returned to baseline activity from 600 ms to 1000 ms to simulate event-related desynchronization (ERD) (Dalal et al., 2008a).

Then, we increased the number of seeded point sources to evaluate the algorithm performance as a function of the number of sources. The locations for the sources were randomly chosen and we also set some minimum distance between sources (at least 15 mm) and a minimum distance from the center of the head (at least 15 mm). The generated time courses were partitioned into control and active periods. The control period (−300 ms to 0 ms, sampled at 1200 Hz) contained only noise and interfering brain activity. The active period of the same length (0 ms to 300 ms, sampled at 1200 Hz) consisted of the activity of interest and interference present in the control period. The SNR was fixed at 5 dB. The number of seeded point sources was increased from two to ten in increments of two for 50 times tests per each configuration. The inter and intra source correlation strengths were set to be 0.95 and 0.95, for more details refer to Owen et al. (2012).

Author Manuscript Author Manuscript Author Manuscript Author Manuscript

Last, we evaluated algorithm performance as a function of SNR. Simulations were performed at SNRs ranging from 0 dB to 20 dB in steps of 5 dB. The estimation of F-ratio performance was evaluated for five randomly seeded point sources with the same configuration as described above for 50 tests. The inter and intra source correlation strengths were set to be 0.95 and 0.95. Again, we set the minimum distance between sources and from the center of the head both at least 15 mm.

3.3. Real datasets

Real MEG data was acquired in the Biomagnetic Imaging Laboratory at University of California, San Francisco (UCSF) with a CTF Omega 2000 whole-head MEG system from VSM MedTech (Coquitlam, BC, Canada) with 1200 Hz sampling rate. The leadfield for each subject was calculated in NUTMEG (Hinkley et al., 2020a) using a single-sphere head model and an 8 mm voxel grid. Each column was normalized to have a norm of unity. Three real MEG data sets were used to evaluate the application of the algorithms: 1. Auditory Evoked Fields (AEF); 2. Finger movement data; 3. Picture naming data. The first two data sets have been reported in our prior publications, and details about the datasets can be found in Wipf et al. (2010a), Dalal et al. (2008a), Owen et al. (2012) for finger movement and picture naming.

We collected 120 trials of AEF data from two subjects; more details related to the task can be found in our prior papers (Cai et al., 2020; 2018). We calculate the change in power from a control time window to the active time window in an extended Alpha band ranging from 4 to 12 Hz (Lehtelä et al., 1997). We set the active window to range from 0 ms to 200 ms, and the baseline window to range from −250 ms to −50 ms. We also collected 96 trials of finger movement data from another subject. We tested the change in power in the Beta and Gamma bands from a control (i.e., baseline) time window to an active time window. For the frequency-domain methods, in Beta band (12–30 Hz), the active window was set to range from −250 to 350 ms and the control window was defined to range from −950 to −750 ms; in the Gamma band (65–90 Hz), the active window was set as −200 to 300 ms and the control window was −900 to −800 ms (Hinkley et al., 2019).

Next, we evaluated the performance of all algorithms on data for the picture naming task. For the visual picture naming test, an image of an object is projected onto a screen (99 trials) and subjects are instructed to name the pictured object verbally; more details can be found in our previous paper (Hinkley et al., 2020b). Again, for the frequency-domain methods, in Beta band (12–30 Hz), the active window was set as −50 to 900 ms and the control window was −200 to 0 ms; in Gamma band (65–90 Hz), the active window was set as −200 to 300 ms and the control window was −150 to −50 ms (Hinkley et al., 2011). Both datasets were processed with a 50 ms window step size.

To evaluate the robustness of TFC to sample size, we evaluate algorithm performance when the number of trials was limited to 10, 20, 40 and 60 for finger movement and picturing name. Based on our previous work (Hinkley et al., 2019), for finger movement task, the active window was set as follows: Beta band 12–30 Hz with active window set to be −50 ms to 150 ms relative to the button press, with −950 ms to −750 ms as the baseline; Gamma band 65–90 Hz with active window set to be 0 ms to 100 ms relative to the button press,

Author Manuscript Author Manuscript Author Manuscript Author Manuscript

with −900 ms to −800 ms as the baseline. For picture naming task, we set the time window and frequencies as follows, Beta band 12–30 Hz with active window set to be −50 ms to 150 ms relative to the button press, with −950 ms to −750 ms as the baseline; Gamma band 65–90 Hz with active window set to be 0 ms to 100 ms relative to the button press, with −900 ms to −800 ms as the baseline. Each test was performed 30 times with the specific trials themselves chosen as a random subset of all available trials (Hinkley et al., 2011). Since there was no existing ground truth for the real tasks, to test robustness and stability of the results, we compare the estimated results with F-ratio estimated with whole trials by TFC during the evaluation. It is worth noting that, even though we apply the TFC as reference ”ground-truth ” here, results are similar when we use TFBF as the reference, because as the number of trials increases performance of TFBF approaches that of TFC.

3.4. Data processing and quantifying algorithm performance

We run TFC in a lattice of time-frequency windows. The original data were first passed through a bank of 200th-order finite impulse response (FIR) bandpass filters and subsequently split into overlapping temporal windows with a step size of 25 ms for all bands. In our filter design, we chose to follow traditional MEG/EEG power band definitions as best as possible. We defined Theta-Alpha band as 4 − 12 Hz with 300 ms windows, Beta band 12 − 30 Hz with 200 ms windows, low Gamma 30 − 55 Hz with 150 ms windows and high Gamma band 65 − 90 Hz with 100 ms windows.

To quantify the performance of TFC and other benchmark algorithms in simulations, in which we knew the ground truth, we used free-response receiver operator characteristics (FROC) which shows the probability for detection of a true source in an image versus the expected value of the number of false positive detections per image (Cai et al., 2018; Darvas et al., 2004; Owen et al., 2012; Sekihara, 2016). Based on the FROC, we compute an A' metric (Cai et al., 2019; Snodgrass and Corwin, 1988), which is an estimate of the area under the FROC curve for each simulation. If the area under the FROC curve is large, then the hit rate is higher compared to the false positive rate. Hit rate (H_R) was calculated by dividing the number of hit point sources by the true number of point sources. The false rate (F_R) was defined by dividing the number of potential false positive voxels by the total number of inactive voxels for each simulation. The details of the A' metric calculation can be perused in our previous paper (Cai et al., 2019). The A' metric ranges from 0 to 1, with higher numbers reflecting better performance (Cai et al., 2018; Darvas et al., 2004; Owen et al., 2012; Sekihara, 2016). To calculate the mean and variance of the A' metric, 50 simulations were conducted for each configuration.

In real data sets, since we did not know the actual brain activity power change, to test the robustness and stability of the results, we compared estimated results with the F-ratio estimated from all trial epochs (120 epochs for AEF data, 96 epochs for finger movement, 99 epochs for picture naming) by TFC for each subject and algorithm. We compared the spatial correlation between estimated F-ratio for a smaller number of trials with the F-ratio estimated for all trial epochs and the results for increasing trial numbers were averaged across 30 simulations for each configuration.

Author Manuscript Author Manuscript Author Manuscript Author Manuscript

4. Results

4.1. Simulation results

In Fig. 1, we show a single example to compare the accuracy of the F-ratio estimation for three simulated point sources. The TFBF was able to provide good results and produce accurate localization for all three sources, the intuition was that the presence of jitter in the source time-course across trials allowed Beamformers to reconstruct source power across trials even if they were highly correlated within a single trial. However, results bled over to other frequency bands and the estimated duration of the activition was longer (greater temporal extent) than the ground truth activation, especially for sources 1 and 2. For sLORETA, the spatial extent of the solution was broader and more blurry for all three simulated sources, with peaks on the periphery of the defined volume of interest in each case. The SNR for sLORETA was also clearly weaker than that of the TFBF solutions. bPCA_TFBF and VBFA_TFBF show similar results as TFBF, and correctly localized all three simulated sources, however, showing some frequency bleed-over and a general overestimation of the temporal duration of the activations of sources 1 and 2. Finally, the results of TFC were superior to those of other benchmarks. TFC was able to localize all three sources, and showed minimal frequency spill-over. The temporal durations of the activation estimated by TFC were more tightly reflecting those of the ground truth compared to other solutions, and produced the highest SNR (color-bar in Fig. 1) in the spectrograms.

Fig. 2 shows the aggregate brain activity power change estimation performance achieved in the simulations. The results of all algorithms as a function of the number of seeded point sources are presented in the left column of Fig. 2. Here, the inter- and intra-source correlation coefficients were fixed to 0.95 and SNR was fixed to 5 dB. All algorithms present the same trend, showing decreasing performance under increasing source count. TFC consistently produced better results than TFBF, bPCA_TFBF, VBFA_TFBF and sLORETA in high correlation settings. bPCA_TFBF and VBFA_TFBF show similar performance, which as slightly inferior to that of TFBF, but both outperformed sLORETA.

Performance as a function of SNR is plotted for all algorithms in the right column of Fig. 2. Reconstruction performance was evaluated for five randomly seeded point sources with both inter- and intra-source correlation coefficients of 0.95. Again, TFC consistently shows better performance than other benchmarks in high correlation settings.

In summary, we demonstrate from simulated data that, while all adaptive beamforming based benchmarks outperform the non-adaptive method-sLORETA, TFC consistently outperforms all benchmarks including adaptive beamformering based methods. Since bPCA_TFBF and VBFA_TFBF show similar performance on the simulated data, we only present the results of VBFA_TFBF on real data in the following.

4.2. Results of real datasets

4.2.1. Auditory evoked field paradigm—Fig. 3 shows auditory evoked field (AEF) localization results obtained using all trials from two subjects. The power change from the control time window to the active time window at each voxel around the M100 peak is plotted for each algorithm. TFBF, sLORETA and VBFA_TFBF failed to generate

Author Manuscript Author Manuscript Author Manuscript Author Manuscript

convincing source solutions, whereas TFC is able to localize the expected bilateral brain activation showing focal reconstructions for both subjects. Specifically, the TFC estimates localize to Heschl's gyrus in the temporal lobe, the location of the primary auditory cortex (A1). These datasets demonstrate that TFC is superior to other source solutions when localizing power changes of highly correlated multiple sources from real data, which is known to be the case for sources in the auditory cortex.

4.2.2. Finger movement data—Fig. 4 shows F-ratios obtained for left index finger movements using different source estimation algorithms. The power change from a control time window to an active time window in the Beta (12–30Hz; Fig. 4, top row) and Gamma bands (65–90Hz; Fig. 4, second row) is superimposed on subject's MRI. As expected, the characteristic Beta band power (12–30 Hz) decrease in contralateral sensorimotor cortex was observed by all algorithms 0–200ms following movement onset. For sLORETA, this solution was blurry (i.e. spatially disperse) and biased towards the edge of the brain in voxels outside of sensorimotor cortex. Additionally, TFBF, VBFA_TFBF and TFC localized a focal high Gamma (65–90 Hz) peak in sensorimotor cortex. This activity was found to be more spatially focal and temporally bound to the movement. For high Gamma, the sLORETA solution was spatially dispersed and not centered on a functionally relevant region for this task (sensorimotor cortex).

Figs. 5 and 6 illustrate the performance of each algorithm using real (left index finger movement) data in Beta and high Gamma bands for increasing numbers of trials. TFC is the only algorithm able to localize a significant Beta band power decrease and a high Gamma peak with as few as ten trials. In contrast, VBFA_TFBF was only able to localize these sources with at least 20 trials, TFBF only localized the same sources with 40 trials, and sLORETA required 60 trials to identify these sources. Overall, TFC outperformed all benchmarks in this dataset with a limited number of trials.

Evaluation of reconstruction algorithm performance against increasing number of trials for left index finger movement data are plotted in Fig. 7. We compared the spatial correlation between the F-ratios as estimated using different algorithms and the F-ratio estimated by TFC using all available trials. While increasing the number of trials increased the performance of all algorithms, TFC outperformed the other solutions for all numbers of trials in both Beta and Gamma bands.

4.2.3. Picture naming task paradigm—Fig. 8 shows the reconstructed power change from the picture naming task obtained by each algorithm from all available trials. TFBF, VBFA_TFBF and TFC were able to localize the visual cortex for the Beta band, similar to our previous findings (Hinkley et al., 2011), while the localization of sLORETA was weighted/biased outside of the cortex and close to the edge of the brain. In the high Gamma band, both TFBF and TFC accurately localized increased power to the primary visual cortices (Hinkley et al., 2011), while other benchmarks localized sources far away (dorsal) from these expected locations. In addition, the localization of TFC was closer to visual cortex and centered around 200ms, confirming the superior spatial and temporal resolution of TFC observed in the simulations.

Author Manuscript Author Manuscript Author Manuscript Author Manuscript

F-ratio results obtained by different algorithms for increasing numbers of trials of the picture naming task in Beta and Gamma bands are shown in Figs. 9 and 10. Similar to the motor data (Figs. 5 and 6), TFC was able to localize Beta power changes to visual cortex with as few as ten trials in a fashion more spatially and temporally focal than other source solutions. Although TFBF and sLORETA perform adequately in reconstructing task-related effects with a few number of trials, activation extents are more broad. Similarly, in high Gamma band, TFC was able to localize power change accurately using all numbers of trials. Source localization for the other solutions were not as accurate in space and time as they were for TFC.

Evaluation results for increasing numbers of trials of the picture naming task are shown in Fig. 11. Similar to what was demonstrated for the motor data, performance of all algorithms increased with increasing numbers of trials, and TFC outperformed all other benchmarks in both the Beta and high Gamma band. Even though sLORETA showed higher spatial correlation than TFBF and VBFA_TFBF for these datasets when the number of trials was less than 40, this gain in performance was lost for sLORETA when the number of trials increased to 40.

In summary, consistent with our expectations from the simulated data, we were able to demonstrate that TFC consistently outperformed other benchmarks in several real datasets. Adaptive beamformer based benchmarks outperformed the non-adaptive method sLORETA, especially for complex brain source power change estimation, which was consistent to our previous findings.

5. Discussion

This paper introduces a novel alternative empirical Bayesian method to localize the time-frequency dynamics of non-phase locked event related cortical activity. Since the proposed algorithm explicitly expands the robust source estimation algorithm, Champagne, we refer to this algorithm as Time-Frequency Champagne (TFC). TFC is able to obtain the spatiotemporal dynamics of cortical oscillations across brain sources and enables the five-dimensional imaging of space, time, and frequency activity in the brain, thereby it is applicable for wide ranging sets of studies of human cortical dynamics during cognition. TFC is able to handle correlated brain activity and resolve many distinct and functionally relevant brain areas, and estimates the minor power changes of brain activity in various tasks even with few trials. TFC displayed significant theoretical and empirical advantages over the existing benchmarks TFBF, bPCA_TFBF, VBFA_TFBF and non adaptive sLORETA. We also demonstrate theoretically that the TFC algorithm can be viewed as a time-frequency optimized beamformer algorithm where model covariances learnt from sparse Bayesian learning are used instead of the sample data covariance.

Simulations were developed to explore the reconstruction performance of complex source configurations with highly correlated time-courses, multiple point sources, and high levels of noise and interference. These simulations demonstrated that TFC outperformed all benchmarks since it showed less frequency bleed-over of activity and the temporal extents of the activations were accurately captured by TFC. In addition, TFC produces highest

Author Manuscript Author Manuscript Author Manuscript Author Manuscript

SNR (colorbar in Fig. 1) in spectrograms and it is more robust to complex brain source reconstruction especially with high correlated time-courses, multiple point sources, and high levels of noise and interference as it show higher A'. In general, it is difficult to evaluate localization algorithm performance with real data since the ground truth is unknown. For this reason, we chose real data sets that have well-established patterns of brain activity (AEF, finger movement data and picture naming task). We also demonstrated that TFC is able to localize the expected bilateral brain activation with focal reconstructions for all subjects for AEF data analysis. TFC was also able to find a characteristic Beta band power decrease in contralateral sensorimotor cortex and a focal high Gamma peak in sensorimotor cortex which confirmed results obtained by our existing robust five dimension beamformer (Dalal et al., 2008a). In a picture naming task analysis, the localization quality of TFC was superior to that of other benchmarks, since the localized voxel was more centered on the time-frequency decomposition and the spread of activation was more restricted. TFC thus not only improved the spatial but also the temporal resolution, yielding the highest output SNR.

Since spontaneous brain activity has a very low signal-to-noise ratio against background activity, many trials are typically required to reconstruct evoked fields. In real data analyses, we also explored the ability of our novel TFC to achieve such reconstructions with few trials. TFC was able to robustly localize brain activity power changes with few trials in the finger movement and picture naming tasks, which can be considered a breakthrough in electromagnetic brain imaging, showing a potential to reduce scanning times for children and other groups of subjects who cannot tolerate long periods of data collection.

Prior efforts in model data covariance estimation have used pure statistical models like probabilistic principal components analysis (PPCA) or factor analysis (FA) models. In our prior work and as benchmarks here, we have demonstrated that such pure statistical model based covariance estimates do not yield robust performance. In contrast, we can view TFC as a hybrid method using a combined biophysical and statistical model that yields robust model covariances which can be used instead of sample covariance estimates in adaptive beamformers.

The robust performance of TFC enables accurate and automated estimation of event related non-phase locked activity from a very small number of trials. Therefore, TFC can significantly advance translational neuroscience studies using MEG imaging. In clinical populations, such as those with neurodevelopmental or neurodegenerative disorders, collecting data with minimal head movements for long scan times can be particularly challenging. In these populations, it may be possible to use TFC with data from shorter scans with fewer number of trials with minimal loss in reconstruction performance.

Algorithm 1

Time Frequency Champagne Algorithm.

Input: Sensor data $\boldsymbol{Y}_C$, $\boldsymbol{Y}_T$ and leadfield matrix $\boldsymbol{L} = [\boldsymbol{L}_1, \ldots, \boldsymbol{L}_N]$

Output: Dynamics of neural activity $\boldsymbol{F}$

Author Manuscript Author Manuscript Author Manuscript Author Manuscript

function TFC($\boldsymbol{Y}_C$, $\boldsymbol{Y}_T$, $\boldsymbol{L}$)

  Filter $\boldsymbol{Y}_C$ and $\boldsymbol{Y}_T$ into several frequency bands $\boldsymbol{Y}_C(f)$ and $\boldsymbol{Y}_T(f)$, $f = 1, \cdots, F$

  for $f = 1, \cdots, F$ **do**

    Segment $\boldsymbol{Y}_T(f)$ into several overlapping windows $\boldsymbol{Y}_T(k, f)$, $(k = 1, \cdots, K)$

    $[\boldsymbol{\Sigma}_C(f), \sim] = \text{CHAMPAGNE}(\boldsymbol{Y}_C(f), \boldsymbol{L})$

    for $k = 1, \cdots, K$ **do**

      $[\boldsymbol{\Sigma}_T(k, f), \sim] = \text{CHAMPAGNE}(\boldsymbol{Y}_T(k, f), \boldsymbol{L})$

      $\boldsymbol{Y}_O(k, f) = [\boldsymbol{Y}_C(f), \boldsymbol{Y}_T(k, f)]$

      $[\boldsymbol{\Sigma}_O(k, f), \boldsymbol{\alpha}_O] = \text{CHAMPAGNE}(\boldsymbol{Y}_O(k, f), \boldsymbol{L})$

      for $n = 1, \cdots, N$ **do**

        if $\alpha_O(n, k, f) \neq 0$ **then**

$$\boldsymbol{F}^{TFC}(n, k, f) = 10 \log_{10} \frac{\text{tr}\left(\boldsymbol{L}_n^\top \boldsymbol{\Sigma}_O^{-1}(k, f) \boldsymbol{\Sigma}_T(k, f) \boldsymbol{\Sigma}_O^{-1}(k, f) \boldsymbol{L}_n\right)}{\text{tr}\left(\boldsymbol{L}_n^\top \boldsymbol{\Sigma}_O^{-1}(k, f) \boldsymbol{\Sigma}_C(f) \boldsymbol{\Sigma}_O^{-1}(k, f) \boldsymbol{L}_n\right)}$$

        else

$$\boldsymbol{F}^{TFC}(n, k, f) = 0$$

        end if

      end for

    end for

  end for

  return $\boldsymbol{F}$

end function

function CHAMPAGNE($\boldsymbol{Y}$, $\boldsymbol{L}$)

  Initialize $\boldsymbol{\alpha} = \text{diag}(\alpha_1 \boldsymbol{I}_{d_c \times d_c}, \cdots, \alpha_N \boldsymbol{I}_{d_c \times d_c})$, $\boldsymbol{\Lambda} = \text{diag}(\lambda_1, \cdots, \lambda_M)$ randomly

  repeat

$$\boldsymbol{\Sigma}_Y = \boldsymbol{L} \boldsymbol{\alpha} \boldsymbol{L}^\top + \boldsymbol{\Lambda}$$

    for $n = 1, \cdots, N$ **do**

$$\bar{\boldsymbol{S}}_n = \hat{\alpha}_n \boldsymbol{L}_n^\top \boldsymbol{\Sigma}_Y^{-1} \boldsymbol{Y}$$

$$\hat{\alpha}_n = \sqrt{\frac{\text{tr}\left(\bar{\boldsymbol{S}}_n^\top \bar{\boldsymbol{S}}_n\right)}{T \text{tr}\left(\boldsymbol{L}_n^\top \boldsymbol{\Sigma}_Y^{-1} \boldsymbol{L}_n\right)}}$$

    end for

    for $m = 1, \cdots, M$ **do**

$$\hat{\lambda}_m = \sqrt{\frac{\left[(\boldsymbol{Y} - \boldsymbol{L}\bar{\boldsymbol{S}})(\boldsymbol{Y} - \boldsymbol{L}\bar{\boldsymbol{S}})^\top\right]_{mm}}{T\left[\boldsymbol{\Sigma}_Y^{-1}\right]_{mm}}}$$

    end for

  until

$$\mathcal{F} = \log|\boldsymbol{\Sigma}_Y| + \text{tr}\left(\boldsymbol{Y}^\top \boldsymbol{\Sigma}_Y^{-1} \boldsymbol{Y}\right) \text{ converges}$$

  return $\boldsymbol{\Sigma}_Y$, $\boldsymbol{\alpha}$

Author Manuscript Author Manuscript Author Manuscript Author Manuscript

36: **end function**

The underlying framework for Bayesian inversion algorithms proposed by Friston et al. (2008), Sato et al. (2004), Belardinelli et al. (2012) et al. is similar to ours. These are all algorithms attempting to parameterize the inverse model in terms of empirical Bayesian estimation of coefficients of covariance components. In the case of Friston et al. (2008). these covariance components are based on spatial bases of the adjacency matrices. In the case of Sato et al. (2004), the covariance components are based on fMRI spatial priors. These approaches can be thought of as estimating multiple sparse priors (MSP) as investigated by Belardinelli et al. (2012). Although our framework is identical to the above publications, there are differences in the exact algorithm for optimization. In contrast to Friston, Sato and Belardinelli et al. who use variations of Restricted Maximum Likelihood, Expectation-Maximization, Fisher Scoring and Greedy Methods with slower and poorer convergence properties, we use a convex-bounding framework with better and faster convergence (see Wipf and Nagarajan, 2009 for details), which also correspond to Majorization Minimization algorithm based on majorization by a convex function using Jesnen's inequality (see recent publication Hashemi et al., 2021b on MM for solving this class of problems). Finally, in contrast to ours and the above mentioned approaches, the approach proposed by Grova et al. (Chowdhury et al., 2013) uses a maximum entropy non-linear framework for source reconstruction and this framework does not have a direct interpretation within a Bayesian framework. Appropriate modifications to these alternative sparse methods could result in similar performance and need to be demonstrated in future work. Related work also includes Gianvittorio et al. who developed a Bayesian method for localization of multiple dipole in the frequency domain (Luria et al., 2019). Future studies should compare their approach with the proposed TFC.

Acknowledgment

The authors would like to thank Danielle Mizuiri and Anne Findlay for collecting much of the MEG data, and all members and collaborators of the Biomagnetic Imaging Laboratory for their support. CC acknowledges support from National Natural Science Foundation of China grant 62007013 and Hubei Provincial Natural Science Foundation of China under Grant 2021CFB384. AH acknowledges scholarship support from the Machine Learning/Intelligent Data Analysis research group at Technische Universität Berlin, the Berlin Mathematical School (BMS) and the Berlin Mathematics Research Center MATH+. SSN acknowledges support from NIH grants R01EB022717, R01DC013979, R01NS10-0440, R01DC176960, R01DC017091, R01AG062196, UCOP-MRP-17-454755, T32EB001631, DOD CDMRP Grant W81XWH1810741, and an industry research contract from Ricoh MEG Inc. SH acknowledges funding from the European Research Council (ERC) under the European Union's Horizon 2020 research and innovation programme (Grant agreement No. 758985).

Appendix A.: Brief summary of the Champagne algorithm

This section briefly introduces the Champagne algorithm with noise learning, for a detailed derivation, we refer to our previous paper (Cai et al., 2020). Champagne algorithm with noise learning is formulated based on an empirical Bayesian schema and the input are only the sensor data $\boldsymbol{Y}$ and leadfiled matrix $\boldsymbol{L}$. Champagne assumes the generative model (Eq. (1)) with the following prior distributions $\boldsymbol{s}(t) \sim \mathcal{N}(\boldsymbol{s}(t) \mid \mathbf{0}, \boldsymbol{\alpha})$ and $\varepsilon(t) \sim \mathcal{N}(0, \boldsymbol{\Lambda})$, where $\boldsymbol{\Lambda} = \mathrm{diag}(\lambda_1, \lambda_2, \cdots, \lambda_M)$ and $\boldsymbol{\alpha}$ is a $d_c N \times d_c N$ block diagonal matrix expressed as $\boldsymbol{\alpha} = \mathrm{diag}(\alpha_1 \boldsymbol{I}_{d_c \times d_c}, \cdots, \alpha_N \boldsymbol{I}_{d_c \times d_c})$, $\alpha_n \boldsymbol{I}_{d_c \times d_c}$ is a prior variance $d_c \times d_c$ matrix of s_n and $\boldsymbol{I}_{d_c \times d_c}$ is a $d_c \times d_c$

Author Manuscript Author Manuscript Author Manuscript Author Manuscript

identity matrix. To estimate the model data covariance, we need to maximize the marginal likelihood expressed below:

$$\mathscr{F} = \log|\boldsymbol{\Sigma}_Y| + \mathrm{tr}\left(\boldsymbol{Y}^\top \boldsymbol{\Sigma}_Y^{-1} \boldsymbol{Y}\right), \tag{A.1}$$

where $\boldsymbol{\Sigma}_Y = \boldsymbol{L}\boldsymbol{\alpha}\boldsymbol{L}^T + \boldsymbol{\Lambda}$ is the model data covariance. The unknown parameters are the prior hyperparameters $\boldsymbol{\alpha}$ and $\boldsymbol{\Lambda}$. Champagne utilizes a convex bounding (Hashemi et al., 2021b; Jordan et al., 1999) on the logarithm of the marginal likelihood (model evidence) to estimate these unknown hyperparameters, which results in the following fast and convergent update rules:

$$\bar{\boldsymbol{S}}_n = \hat{\alpha}_n \boldsymbol{L}_n^\top \boldsymbol{\Sigma}_Y^{-1} \boldsymbol{Y}, \tag{A.2}$$

$$\hat{\alpha}_n = \sqrt{\frac{\mathrm{tr}\left(\bar{\boldsymbol{S}}_n^\top \bar{\boldsymbol{S}}_n\right)}{T\,\mathrm{tr}\left(\boldsymbol{L}_n^\top \boldsymbol{\Sigma}_Y^{-1} \boldsymbol{L}_n\right)}}, \tag{A.3}$$

$$\hat{\lambda}_m = \sqrt{\frac{\left[(\boldsymbol{Y} - \boldsymbol{L}\bar{\boldsymbol{S}})(\boldsymbol{Y} - \boldsymbol{L}\bar{\boldsymbol{S}})^\top\right]_{mm}}{T\left[\boldsymbol{\Sigma}_Y^{-1}\right]_{mm}}}. \tag{A.4}$$

In short, the Champagne algorithm with noise learning first initializes the voxel variances and noise covariance with random values, then updates the voxel variances and the noise covariance using Eqs. (A.2), (A.3) and (A.4) until the cost function Eq. (A.1) converges. Finally, the Champagne algorithm with noise learning outputs the model data covariance $\boldsymbol{\Sigma}_Y$, brain source activity $\bar{\boldsymbol{S}}$ and estimated prior distributions variance $\hat{\boldsymbol{\alpha}}$.

For robust estimation of source power for control and time windows using the Champagne algorithm, we start by filtering and segmenting the sensor data into control time and K task time windows, to calculate the change from control time window $\boldsymbol{Y}_C(f)$ to k-th task time window $\boldsymbol{Y}_T(k, f)$. To ensure that the magnitude of sources are comparable between the task and control periods and decreases the likelihood of resolving false sources, we run Champagne algorithm with the input of omnibus data that includes both task and control time-windows, denoted as $\boldsymbol{Y}_O(k, f) = [\boldsymbol{Y}_C(f), \boldsymbol{Y}_T(k, f)]$ and leadfield matrix $\boldsymbol{L}$ to obtain omnibus prior hyperparamters $\boldsymbol{\alpha}_O(k, f)$ and model data covariance $\boldsymbol{\Sigma}_O(K, f)$. We then use the omnibus parameters to estimate the source power in control and task periods at n-th voxel (Eqs. (3) and (4) in the main paper) expressed as

$$\begin{aligned}\widehat{P}_C(n, k, f) &= \mathrm{tr}\left[E_{p(\boldsymbol{S}_C \mid \boldsymbol{Y}_C)}\left[(\boldsymbol{S}_C)_n (\boldsymbol{S}_C^\top)_n\right]\right] \\ &= \alpha_O^2(n, k, f)\mathrm{tr}\left(\boldsymbol{L}_n^\top \boldsymbol{\Sigma}_O^{-1}(k, f)\boldsymbol{\Sigma}_C(f)\boldsymbol{\Sigma}_O^{-1}(k, f)\boldsymbol{L}_n\right),\end{aligned} \tag{A.5}$$

$$\begin{aligned}\widehat{P}_T(n, k, f) &= \mathrm{tr}\left[E_{p(\boldsymbol{S}_T \mid \boldsymbol{Y}_T)}\left[(\boldsymbol{S}_T)_n (\boldsymbol{S}_T^\top)_n\right]\right] \\ &= \alpha_O^2(n, k, f)\mathrm{tr}\left(\boldsymbol{L}_n^\top \boldsymbol{\Sigma}_O^{-1}(k, f)\boldsymbol{\Sigma}_T(k, f)\boldsymbol{\Sigma}_O^{-1}(k, f)\boldsymbol{L}_n\right),\end{aligned} \tag{A.6}$$

Author Manuscript Author Manuscript Author Manuscript Author Manuscript

where $\mathbf{\Sigma}_C(f)$ and $\mathbf{\Sigma}_T(k, f)$ are well-regularized model covariances of control and task windows estimated by running Champagne algorithm with inputs $\boldsymbol{Y}_C(f)$, $\boldsymbol{L}$ and $\boldsymbol{Y}_T(k, f)$.

Appendix B.: Bayesian Principal Components Analysis (bPCA) and Factor Analysis (FA) estimates of model data covariance

Bayesian PCA (bPCA) corresponds to a multivariate Gaussian model where a random vector can be expressed as a weighted linear combination of random components superimposed by independent noise. The covariance can be decomposed as the sum of a low rank matrix and a scaled identity matrix. With this statistical model, standard PCA is transformed into a latent variable model such as VBFA.

To derive the bPCA model, we use an extension of the standard bPCA model (Engemann and Gramfort, 2015; Nagarajan et al., 2007; Woolrich et al., 2011). We assume K represents the number of components and $\boldsymbol{Y}$ a sample sensor time series. The M-dimensional vector $\boldsymbol{Y}$ is then obtained from a K-dimensional random vector $\boldsymbol{X}$ which is linearly transformed by K latent factors forming a matrix $\boldsymbol{A}$ of size $M \times K$, and a random noise vector ϵ. The generative model used in bPCA is then expressed as:

$$\boldsymbol{Y} = \boldsymbol{A}\boldsymbol{X} + \epsilon, \tag{B.1}$$

where we assume that both $\boldsymbol{X}$ and ϵ are mutually independent random vectors drawn from spherical multivariate Gaussian distributions, of respective dimensionalities K and M. Without loss of generality, the prior distributions of $\boldsymbol{X}$ and ϵ are assumed as:

$$p(\boldsymbol{X}) = \mathcal{N}(\mathbf{0}, \boldsymbol{I}), \tag{B.2}$$

$$p(\epsilon) = \mathcal{N}\left(\mathbf{0}, \sigma^{-1}\boldsymbol{I}\right). \tag{B.3}$$

The prior on $\boldsymbol{A}$ is an automatic relevance determination (ARD) prior:

$$p(\boldsymbol{A}) = \mathcal{N}\left(\mathbf{0}, (\sigma\Psi)^{-1}\right), \tag{B.4}$$

where $\sigma\boldsymbol{I}$ and $\sigma\Psi$ are the prior precision of noise ϵ and weight matrix $\boldsymbol{A}$. Using Variational Bayes (VB) inference to approximate the unknown parameters $\boldsymbol{A}$, $\boldsymbol{X}$, σ and Ψ by maximizing the variational free energy, the update rules are as follows,

$$\begin{aligned}
\boldsymbol{A} &= \boldsymbol{R}_{YX}(\boldsymbol{R}_{XX} + \Psi)^{-1}, \\
\boldsymbol{X} &= \sigma\left[\boldsymbol{A}^{\top}\sigma\boldsymbol{A} + M(\boldsymbol{R}_{XX} + \Psi)^{-1} + I\right]^{-1}\boldsymbol{A}\boldsymbol{Y}, \\
\sigma &= \frac{1}{KM}\mathrm{tr}(\boldsymbol{R}_{YY} - \boldsymbol{A}\boldsymbol{R}_{YX}), \\
\Psi &= \mathrm{diag}\left[\frac{1}{M}\boldsymbol{A}^{\top}\sigma\boldsymbol{A} + (\boldsymbol{R}_{XX} + \Psi)^{-1}\right],
\end{aligned} \tag{B.5}$$

Author Manuscript Author Manuscript Author Manuscript Author Manuscript

where, $\boldsymbol{R_{YY}}$ is the sample data covariance of $\boldsymbol{Y}$, $\boldsymbol{R_{YX}}$ and $\boldsymbol{R_{YX}}$ are the expected data covariance of $\boldsymbol{YX}$ and $\boldsymbol{XX}$ Sekihara and Nagarajan (2015). After convergence, the covariance derived from the bPCA model is given by:

$$\boldsymbol{\Sigma}_{\boldsymbol{Y}}^{bPCA} = \boldsymbol{A}\boldsymbol{A}^{\top} + \sigma \boldsymbol{I}_{M}\,. \tag{B.6}$$

We note that the model used for bPCA in Eq. (B.4) can be considered as a special case of the model used in Factor Analysis. In bPCA, the error, ϵ is assumed to be a homoscedastic noise, $\epsilon \sim \mathcal{N}(0, \sigma \boldsymbol{I}_{M})$: the noise variance is the same for all variables, here all sensors. In contrast, FA assumes a heteroscedastic noise, $\epsilon \sim \mathcal{N}(0, \boldsymbol{\Sigma}_{\epsilon})$, where $\boldsymbol{\Sigma}_{\epsilon} = \mathrm{diag}(\sigma_1, \cdots, \sigma_M)$: the noise variance differs between sensors. In this case, the update rule of Σ_{ϵ} is expressed as $\boldsymbol{\Sigma}_{\epsilon} = \frac{1}{K}\mathrm{diag}(\boldsymbol{R_{YY}} - \boldsymbol{A}\boldsymbol{R_{YX}})$. The estimated model data covariance as delivered by FA is given by

$$\boldsymbol{\Sigma}_{\boldsymbol{Y}}^{FA} = \boldsymbol{A}\boldsymbol{A}^{\top} + \boldsymbol{\Sigma}_{\epsilon}\,. \tag{B.7}$$

This estimate of the model data covariance (Eqs. (B.6) and (B.7)) can be used to compute the beamformer weights and the estimated source power, and finally the F-ratio of the power contrast. In this paper, we named Time_Frequency Beamformer with model covariance learnt by bPCA and VBFA as bPCA_TFBF and VBFA_TFBF.

References

Al-Shoukairi M, Rao BD, 2019. Sparse signal recovery using mpdr estimation. In: ICASSP 2019–2019 IEEE International Conference on Acoustics, Speech and Signal Processing (ICASSP). IEEE, pp. 5047–5051.

Belardinelli P, Ortiz E, Barnes G, Noppeney U, Preissl H, 2012. Source reconstruction accuracy of MEG and EEG bayesian inversion approaches. PloS one 7 (12), e51985.

Borghesani V, Hinkley LB, Ranasinghe KG, Thompson MM, Shwe W, Mizuiri D, Lauricella M, Europa E, Honma S, Miller Z, et al. , 2020. Taking the sublexical route: brain dynamics of reading in the semantic variant of primary progressive aphasia. Brain 143 (8), 2545–2560. [PubMed: 32789455]

Brookes MJ, Stevenson CM, Barnes GR, Hillebrand A, Simpson MI, Francis ST, Morris PG, 2006. Beamformer reconstruction of correlated sources using a modified source model. NeuroImage 34. 1454–65 [PubMed: 17196835]

Cai C, Diwakar M, Chen D, Sekihara K, Nagarajan SS, 2019. Robust Empirical Bayesian Reconstruction of Distributed Sources for Electromagnetic Brain Imaging. IEEE Transactions on Medical Imaging 39 (3), 567–577. [PubMed: 31380750]

Cai C, Hashemi A, Diwakar M, Haufe S, Sekihara K, Nagarajan SS, 2020. Robust estimation of noise for electromagnetic brain imaging with the Champagne algorithm. NeuroImage 225, 117411.

Cai C, Hashemi A, Diwakar M, Haufe S, Sekihara K, Nagarajan SS, 2021. Robust estimation of noise for electromagnetic brain imaging with the Champagne algorithm. NeuroImage 225, 117411.

Cai C, Sekihara K, Nagarajan SS, 2018. Hierarchical multiscale Bayesian algorithm for robust MEG/EEG source reconstruction. NeuroImage 183, 698–715. [PubMed: 30059734]

Chowdhury RA, Lina JM, Kobayashi E, Grova C, 2013. MEG source localization of spatially extended generators of epileptic activity: comparing entropic and hierarchical bayesian approaches. PloS one 8 (2), e55969.

Dalal SS, Guggisberg AG, Edwards E, Sekihara K, Findlay AM, Canolty RT, Berger MS, Knight RT, Barbaro NM, Kirsch HE, Nagarajan SS, 2008. Five-dimensional neuroimaging: Localization of the time-frequency dynamics of cortical activity. NeuroImage 40, 1686–1700. [PubMed: 18356081]

Author Manuscript Author Manuscript Author Manuscript Author Manuscript

Dalal SS, Guggisberg AG, Edwards E, Sekihara K, Findlay AM, Canolty RT, Berger MS, Knight RT, Barbaro NM, Kirsch HE, et al. , 2008. Five-dimensional neuroimaging: localization of the time–frequency dynamics of cortical activity. Neuroimage 40 (4), 1686–1700. [PubMed: 18356081]

Dalal SS, Sekihara K, Nagarajan SS, 2006. Modified beamformers for coherent source region suppression. IEEE Trans. Biomed. Eng 53. 1357–63 [PubMed: 16830939]

Dalal SS, Zumer J, Agrawal V, Hild K, Sekihara K, Nagarajan S, 2004. NUTMEG: a neuromagnetic source reconstruction toolbox. Neurology & clinical neurophysiology: NCN 2004, 52. [PubMed: 16012626]

Darvas F, Pantazis D, Kucukaltun-Yildirim E, Leahy R, 2004. Mapping human brain function with MEG and EEG: methods and validation. NeuroImage 23, S289–S299. [PubMed: 15501098]

Diwakar M, Huang MX, Srinivasan R, Harrington DL, Robb A, Angeles A, Muzzatti L, Pakdaman R, Song T, Theilmann RJ, Lee RR, 2010. Dual-core beamformer for obtaining highly correlated neuronal networks in meg. NeuroImage 54, 253–263. [PubMed: 20643211]

Diwakar M, Tal O, Liu TT, Harrington DL, Srinivasan R, Muzzatti L, Song T, Theilmann RJ, Lee RR, Huang MX, 2011. Accurate reconstruction of temporal correlation for neuronal sources using the enhanced dual-core MEG beamformer. NeuroImage 56. 1918–28 [PubMed: 21443954]

van Drongelen W, Yuchtman M, van Veen BD, van Huffelen AC, 1996. A spatial filtering technique to detect and localize multiple sources in the brain. Brain Topography 9, 39–49.

Engemann DA, Gramfort A, 2015. Automated model selection in covariance estimation and spatial whitening of MEG and EEG signals. NeuroImage 108, 328–342. [PubMed: 25541187]

Friston K, Harrison L, Daunizeau J, Kiebel S, Phillips C, Trujillo-Barreto N, Henson R, Flandin G, Mattout J, 2008. Multiple sparse priors for the M/EEG inverse problem. NeuroImage 39 (3), 1104–1120. doi: 10.1016/j.neuroimage.2007.09.048. [PubMed: 17997111]

Gramfort A, Strohmeier D, Haueisen J, Hämäläinen MS, Kowalski M, 2013. Time-frequency mixed-norm estimates: Sparse M/EEG imaging with non-stationary source activations. NeuroImage 70, 410–422. [PubMed: 23291276]

Gross J, Kujala J, Hämäläinen M, Timmermann L, Schnitzler A, Salmelin R, 2001. Dynamic imaging of coherent sources: studying neural interactions in the human brain. Proceedings of the National Academy of Sciences 98 (2), 694–699.

Gross J, Timmermann L, Kujala J, Salmelin R, Schnitzler A, 2003. Properties of MEG tomographic maps obtained with spatial filtering. NeuroImage 19, 1329–1336. [PubMed: 12948691]

Guggisberg AG, Kirsch HE, Mantle MM, Barbaro NM, Nagarajan SS, 2008. Fast oscillations associated with interictal spikes localize the epileptogenic zone in patients with partial epilepsy. Neuroimage 39 (2), 661–668. [PubMed: 17977022]

Hallez H, Vanrumste B, Grech R, Muscat J, De Clercq W, Vergult A, D'Asseler Y, Camilleri KP, Fabri SG, Van Huffel S, et al. , 2007. Review on solving the forward problem in EEG source analysis. Journal of neuroengineering and rehabilitation 4 (1), 46. [PubMed: 18053144]

Hämäläinen MS, Ilmoniemi RJ, 1994. Interpreting magnetic fields of the brain: minimum norm estimates. Medical & biological engineering & computing 32 (1), 35–42. [PubMed: 8182960]

Hashemi A, Cai C, Gao Y, Ghosh S, Müller K-R, Nagarajan S, Haufe S, 2021. Joint Learning of Full-structure Noise in Hierarchical Bayesian Regression Models. bioRxiv doi: 10.1101/2021.11.28.470264.

Hashemi A, Cai C, Kutyniok G, Müller K-R, Nagarajan S, Haufe S, 2021. Unification of sparse Bayesian learning algorithms for electromagnetic brain imaging with the majorization minimization framework. NeuroImage 239, 118309.

Hashemi A, Gao Y, Cai C, Ghosh S, Müller KR, Nagarajan SS, Haufe S, 2021. Efficient hierarchical Bayesian inference for spatio-temporal regression models in neuroimaging. In: Thirty-Fifth Conference on Neural Information Processing Systems.

Hashemi A, Haufe S, 2018. Improving EEG Source Localization through Spatio-temporal Sparse Bayesian Learning. Submitted to 26th European Signal Processing Conference (EUSIPCO).

Herman AB, Houde JF, Vinogradov S, Nagarajan SS, 2013. Parsing the phonological loop: activation timing in the dorsal speech stream determines accuracy in speech reproduction. Journal of Neuroscience 33 (13), 5439–5453. [PubMed: 23536060]

Author Manuscript Author Manuscript Author Manuscript Author Manuscript

Hinkley LB, Dale CL, Cai C, Zumer J, Dalal S, Findlay A, Sekihara K, Nagarajan SS, 2020. NUTMEG: Open Source Software for M/EEG Source Reconstruction. Frontiers in Neuroscience 14, 710. [PubMed: 32982658]

Hinkley LB, Dale CL, Luks TL, Findlay AM, Bukshpun P, Pojman N, Thieu T, Chung WK, Berman J, Roberts TP, et al. , 2019. Sensorimotor cortical oscillations during movement preparation in 16p11. 2 deletion carriers. Journal of Neuroscience 39 (37), 7321–7331. [PubMed: 31270155]

Hinkley LB, De Witte E, Cahill-Thompson M, Mizuiri D, Garrett C, Honma S, Findlay A, Gorno-Tempini ML, Tarapore P, Kirsch HE, et al. , 2020. Optimizing Magnetoencephalographic Imaging Estimation of Language Lateralization for Simpler Language Tasks. Frontiers in Human Neuroscience 14.

Hinkley LB, Nagarajan SS, Dalal SS, Guggisberg AG, Disbrow EA, 2011. Cortical temporal dynamics of visually guided behavior. Cerebral Cortex 21 (3), 519–529. [PubMed: 20601397]

Jordan MI, Ghahramani Z, Jaakkola TS, Saul LK, 1999. An introduction to variational methods for graphical models. Machine learning 37 (2), 183–233.

Lehtelä L, Salmelin R, Hari R, 1997. Evidence for reactive magnetic 10-hz rhythm in the human auditory cortex. Neuroscience letters 222 (2), 111–114. [PubMed: 9111741]

Limpiti T, Van Veen BD, Attias HT, Nagarajan SS, 2008. A spatiotemporal framework for estimating trial-to-trial amplitude variation in event-related MEG/EEG. IEEE Transactions on Biomedical Engineering 56 (3), 633–645. [PubMed: 19272883]

Luria G, Duran D, Visani E, Sommariva S, Rotondi F, Sebastiano DR, Panzica F, Piana M, Sorrentino A, 2019. Bayesian multi-dipole modelling in the frequency domain. Journal of neuroscience methods 312, 27–36. [PubMed: 30452978]

Nagarajan SS, Attias HT, Hild KE, Sekihara K, 2007. A probabilistic algorithm for robust interference suppression in bioelectromagnetic sensor data. Statistics in Medicine 26. 3886–910 [PubMed: 17546712]

Owen JP, Wipf DP, Attias HT, Sekihara K, Nagarajan SS, 2012. Performance evaluation of the champagne source reconstruction algorithm on simulated and real M/EEG data. Neuroimage 60 (1), 305–323. [PubMed: 22209808]

Pascual-Marqui RD, 2002. Standardized low resolution brain electromagnetic tomography (sLORETA): technical details. Methods and Findings in Experimental and Clinical Pharmacology 24, 5–12. [PubMed: 12575463]

Pote RR, Rao BD, 2020. Robustness of sparse Bayesian Learning in Correlated Environments. In: ICASSP 2020–2020 IEEE International Conference on Acoustics, Speech and Signal Processing (ICASSP). IEEE, pp. 9100–9104.

Ranasinghe KG, Petersen C, Kudo K, Srivatsan S, Beagle AJ, Mizuiri D, Findlay A, Houde JF, Rankin K, Rabinovici GD, et al. , 2020. Alpha-frequency synchronization deficits during life predict postmortem neurofibrillary tangle burden in alzheimer's disease: Biomarkers: Leveraging postmortem collections to validate neuroimaging. Alzheimer's & Dementia 16, e045351.

Robinson S, Vrba J, 1999. Functional neuroimaging by synthetic aperture magnetometry (sam). Recent Advances in Biomagnetism,In: Yoshimoto T, Kotani M, Kuriki S, Karibe H. and Nakasato N, Eds. 302–305.

Sato M. a., Yoshioka T, Kajihara S, Toyama K, Goda N, Doya K, Kawato M, 2004. Hierarchical Bayesian estimation for MEG inverse problem. NeuroImage 23 (3), 806–826. [PubMed: 15528082]

Schmidt RO, 1986. Multiple emitter location and signal parameter estimation. IEEE Trans. Antenn. Propagat 34, 276–280.

Sekihara K, 2016. Computing Resolution for Neuromagnetic Imaging Systems. J Comput Eng Inf Technol 5: 3. doi: 10.4172/23249307,2.

Sekihara K, Nagarajan SS, 2015. Electromagnetic brain imaging: A Bayesian perspective. Springer-Verlag, Berlin, Heidelber.

Sekihara K, Nagarajan SS, Poeppel D, Marantz A, Miyashita Y, 2001. Reconstructing spatio-temporal activities of neural sources using an MEG vector beamformer technique. IEEE Trans. Biomed. Eng 48, 760–771. [PubMed: 11442288]

Author Manuscript Author Manuscript Author Manuscript Author Manuscript

Singh KD, Barnes GR, Hillebrand A, 2003. Group imaging of task-related changes in cortical synchronisation using nonparametric permutation testing. Neuroimage 19 (4), 1589–1601. [PubMed: 12948714]

Snodgrass JG, Corwin J, 1988. Pragmatics of measuring recognition memory: applications to dementia and amnesia. Journal of Experimental Psychology: General 117 (1), 34. [PubMed: 2966230]

Stoica P, Nehorai A, 1990. MUSIC, maximum likelihood, and cramer-rao bound: further results and comparisons. IEEE Trans. Acoust. Speech Signal Process 38, 2140–2150.

Uutela K, Hämäläinen M, Somersalo E, 1999. Visualization of magnetoencephalographic data using minimum current estimate. NeuroImage 10, 173–180. [PubMed: 10417249]

Van Veen BD, Van Drongelen W, Yuchtman M, Suzuki A, 1997. Localization of brain electrical activity via linearly constrained minimum variance spatial filtering. IEEE Trans. Biomed. Eng 44, 867–880. [PubMed: 9282479]

Velmurugan J, Nagarajan SS, Mariyappa N, Mundlamuri RC, Raghavendra K, Bharath RD, Saini J, Arivazhagan A, Rajeswaran J, Mahadevan A, et al. , 2019. Magnetoencephalography imaging of high frequency oscillations strengthens presurgical localization and outcome prediction. Brain 142 (11), 3514–3529. [PubMed: 31553044]

Vrba J, Robinson SE, 2001. Signal processing in magnetoencephalography. Methods 25 (2), 249–271. [PubMed: 11812209]

Wipf D, Nagarajan S, 2009. A unified bayesian framework for MEG/EEG source imaging. NeuroImage 44 (3), 947–966. [PubMed: 18602278]

Wipf DP, Owen JP, Attias HT, Sekihara K, Nagarajan SS, 2010. Robust Bayesian estimation of the location, orientation, and time course of multiple correlated neural sources using MEG. NeuroImage 49, 641–655. [PubMed: 19596072]

Wipf DP, Owen JP, Attias HT, Sekihara K, Nagarajan SS, 2010. Robust bayesian estimation of the location, orientation, and time course of multiple correlated neural sources using MEG. NeuroImage 49 (1), 641–655. [PubMed: 19596072]

Woolrich M, Hunt L, Groves A, Barnes G, 2011. MEG beamforming using Bayesian PCA for adaptive data covariance matrix regularization. Neuroimage 57 (4), 1466–1479. [PubMed: 21620977]

Author Manuscript Author Manuscript Author Manuscript Author Manuscript

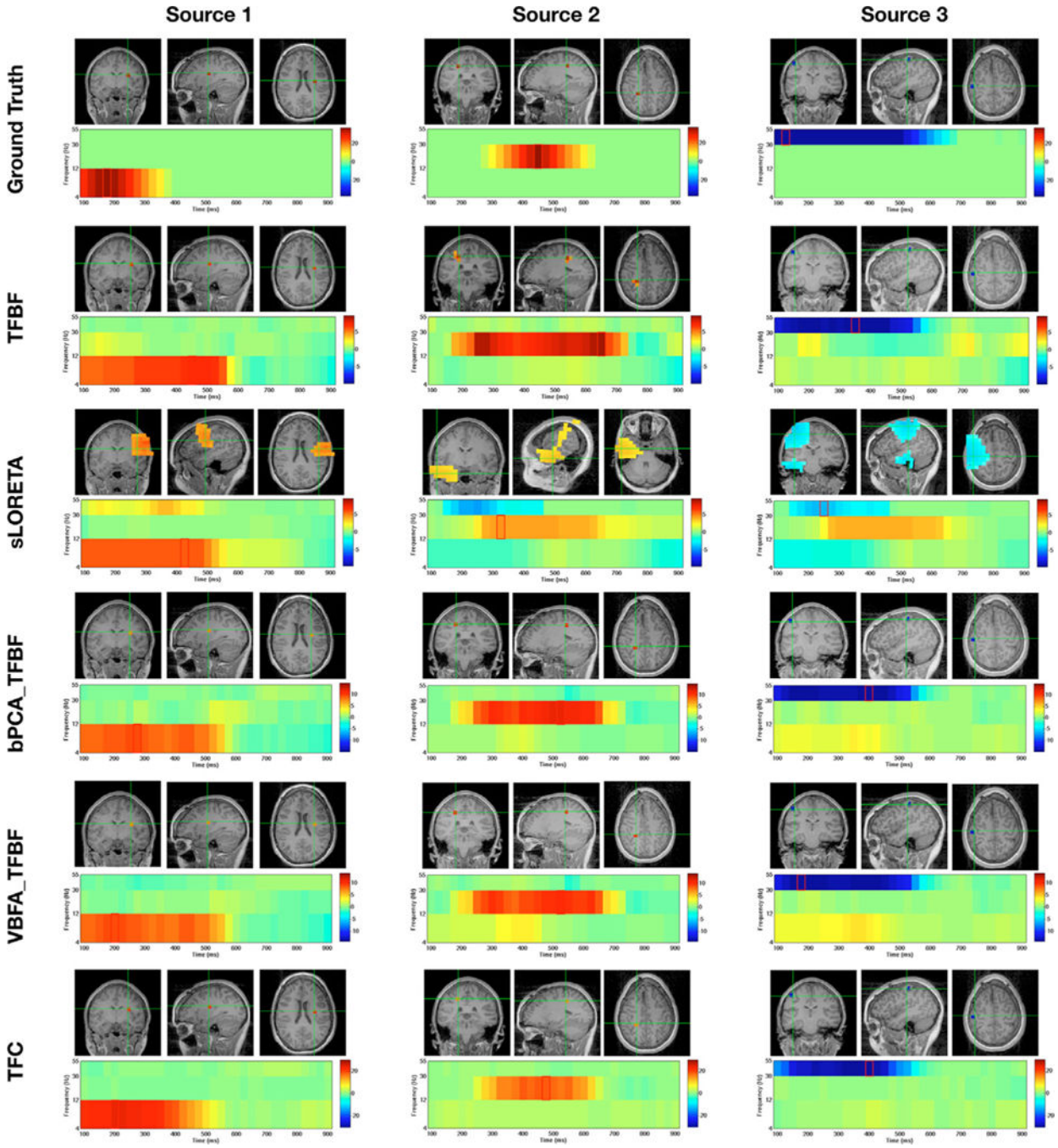

Fig. 1.

A single example to compare the performance of F-ratio estimation across methods. Shown at the top are the peaks and corresponding spectrograms of the three simulated sources. In the rows below the reconstruction results using TFBF, sLORETA, bPCA_TFBF, VBFA_TFBF and TFC are shown. In each of those panels, the crosshairs mark the spatiotemporal peak of the F-ratio for the reconstructed source, with the corresponding spectrogram shown below it. The time-frequency window for which the spatial activation map is superimposed on the MRI is highlighted in the spectrogram.

Author Manuscript Author Manuscript Author Manuscript Author Manuscript

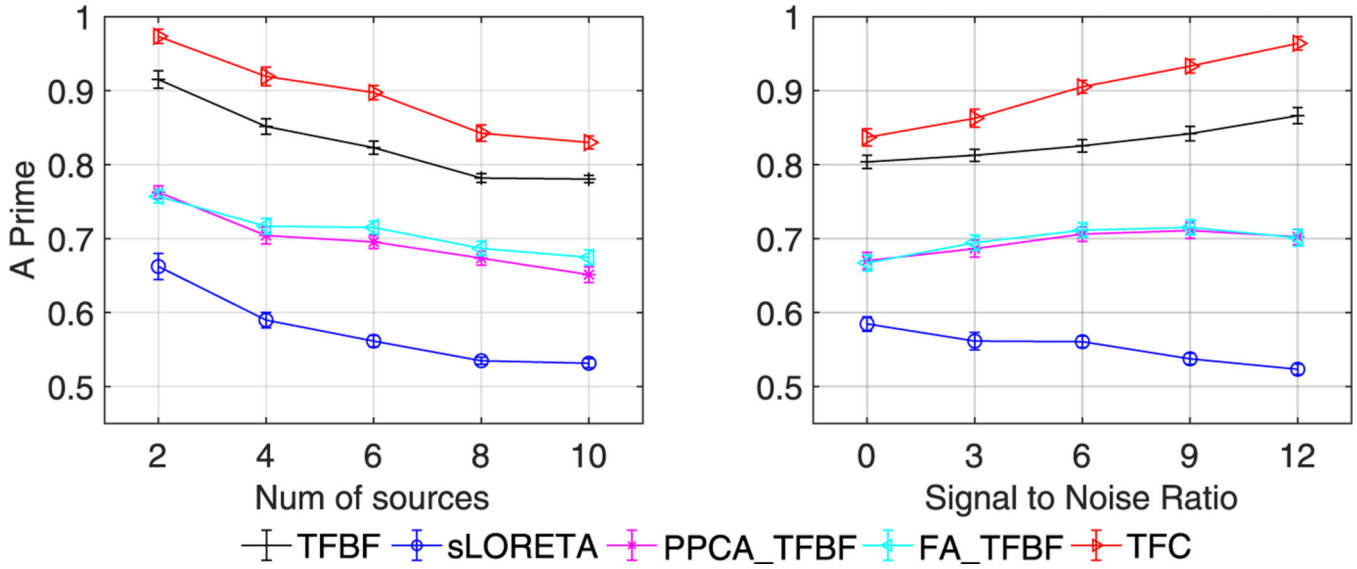

Fig. 2.

Localization results of aggregate performance as a function of the number of seeded point sources and the signal-to-noise ratio. The inter- and intra- source correlation were set to 0.95 and 0.95. The results are averaged across 50 simulations for each configuration and the error bars represent the standard error.

Author Manuscript Author Manuscript Author Manuscript Author Manuscript

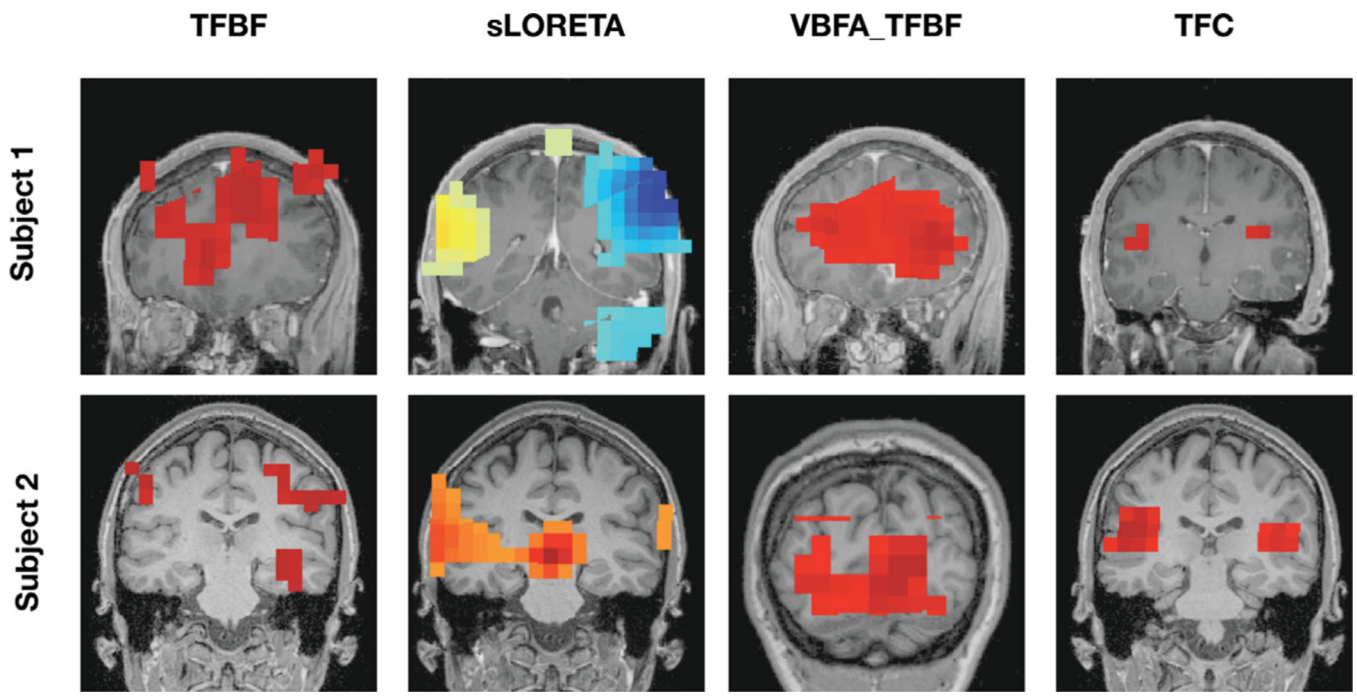

Fig. 3.

Auditory evoked field (AEF) results for two subjects obtained for all available trials. The results using TFC are shown in the right-most column and the results obtained using the benchmark algorithms are shown in the other four columns.

Author Manuscript

Author Manuscript

Author Manuscript

Author Manuscript

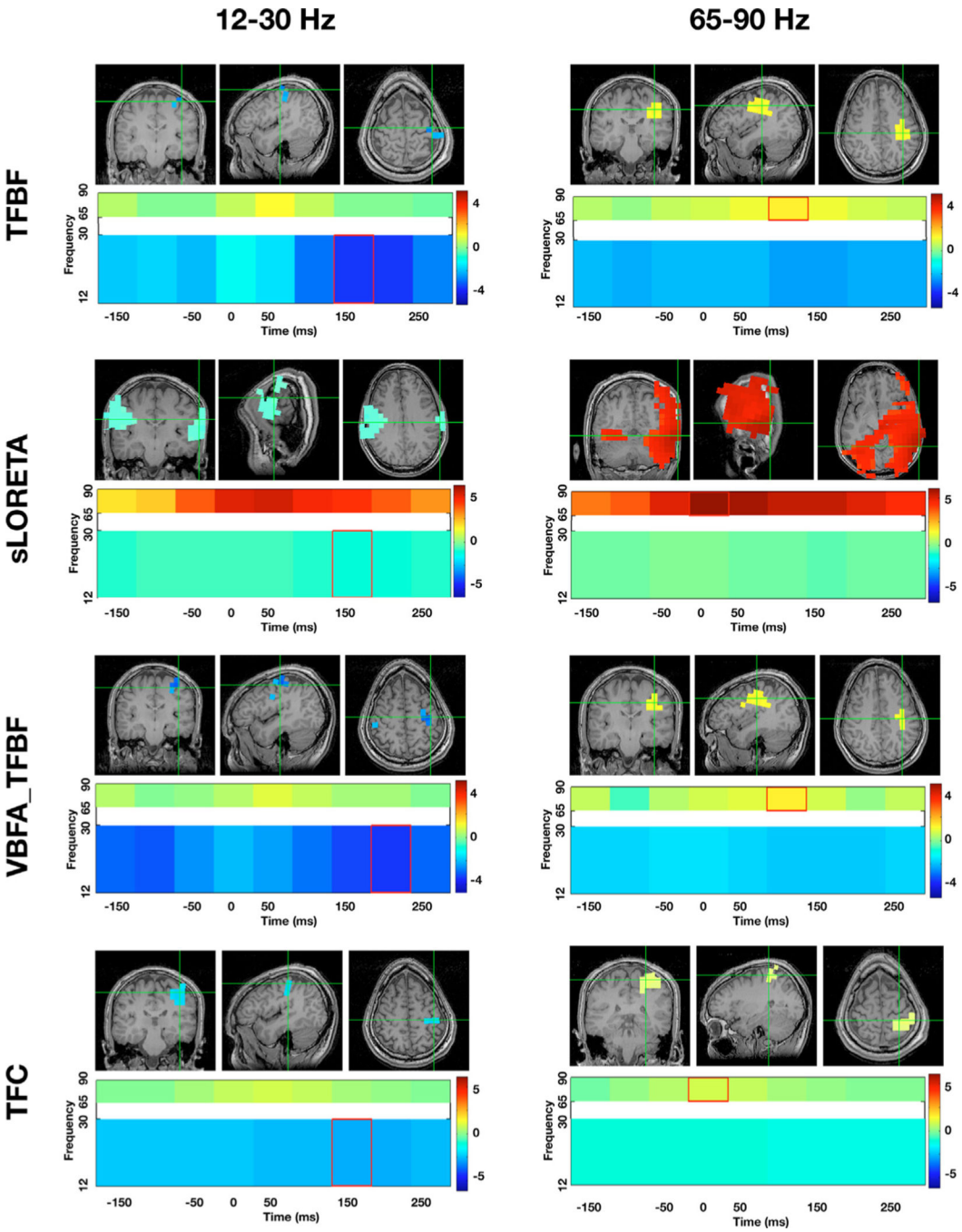

Fig. 4.

Shown above are F-ratios obtained for left index finger movement data using different algorithms. The change in power from a control time window to an active time window was superimposed on subject's brain for the Beta (first row) and Gamma bands (second row).

Author Manuscript Author Manuscript Author Manuscript Author Manuscript

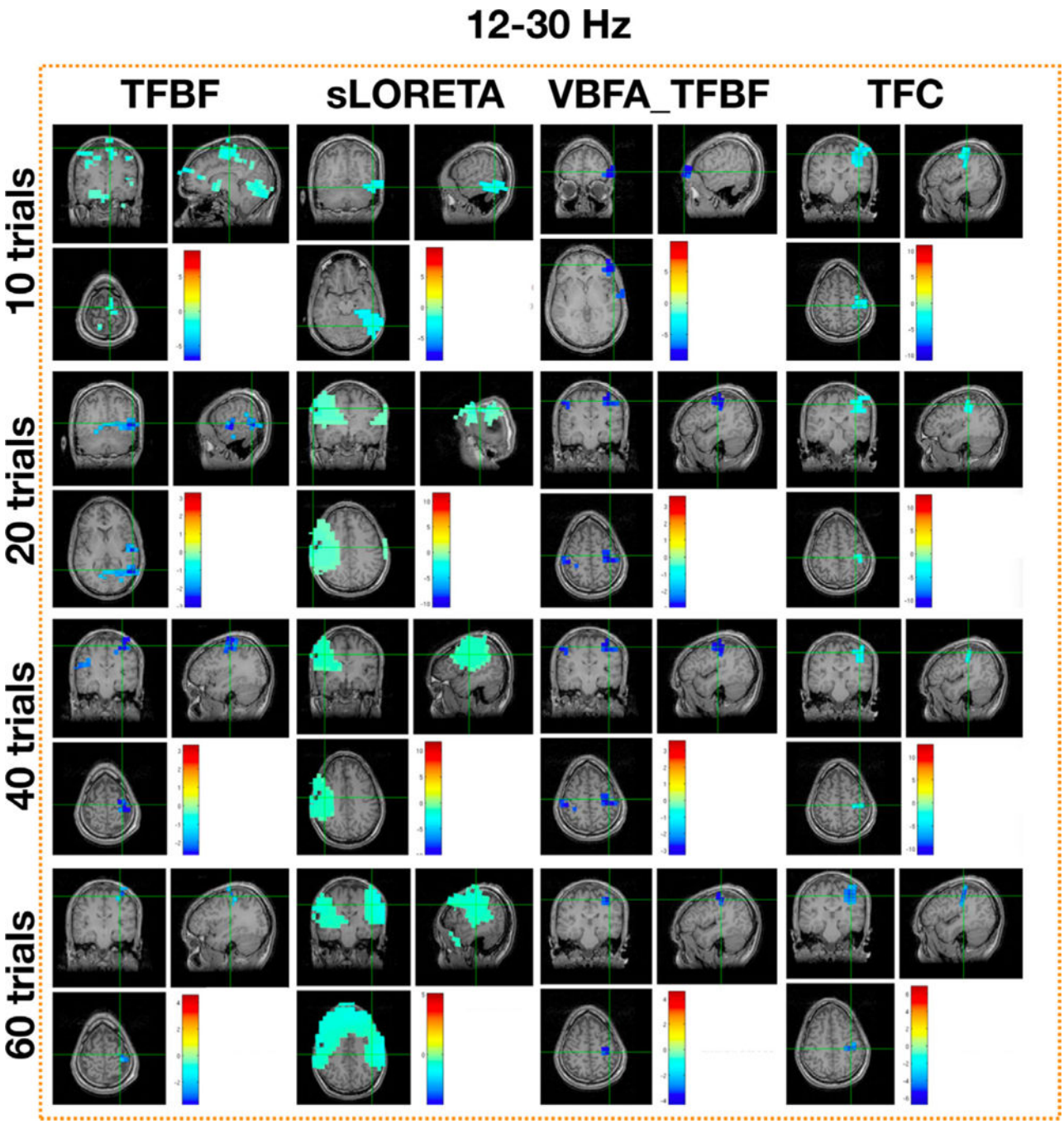

Fig. 5.

Single example showing F-ratios for left index finger movement in Beta band obtained for different algorithms as a function of the number of trials.

Author Manuscript Author Manuscript Author Manuscript Author Manuscript

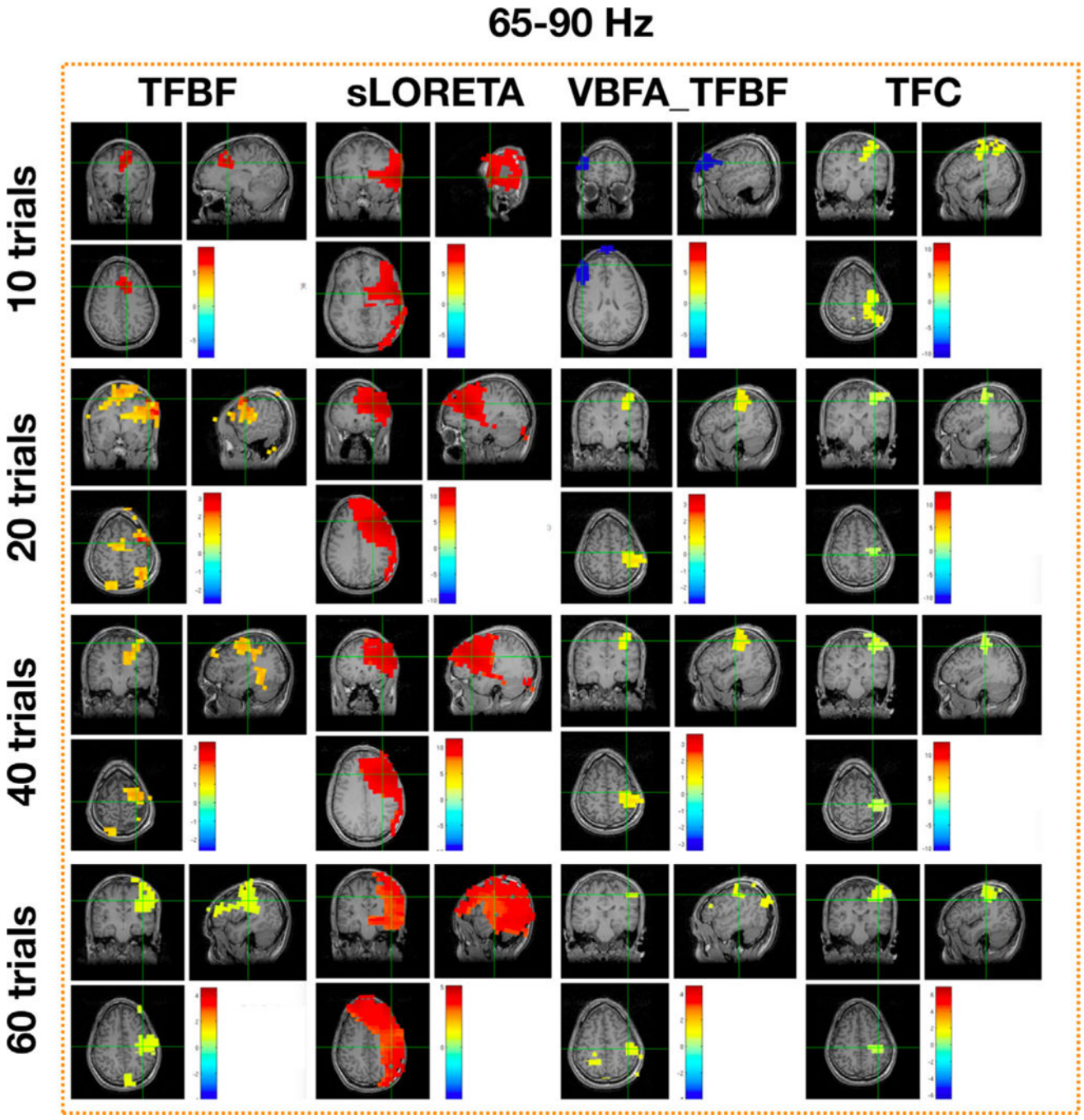

Fig. 6.

Single example showing F-ratios for left index finger movement in high Gamma band obtained for different algorithms as a function of the number of trials.

Author Manuscript Author Manuscript Author Manuscript Author Manuscript

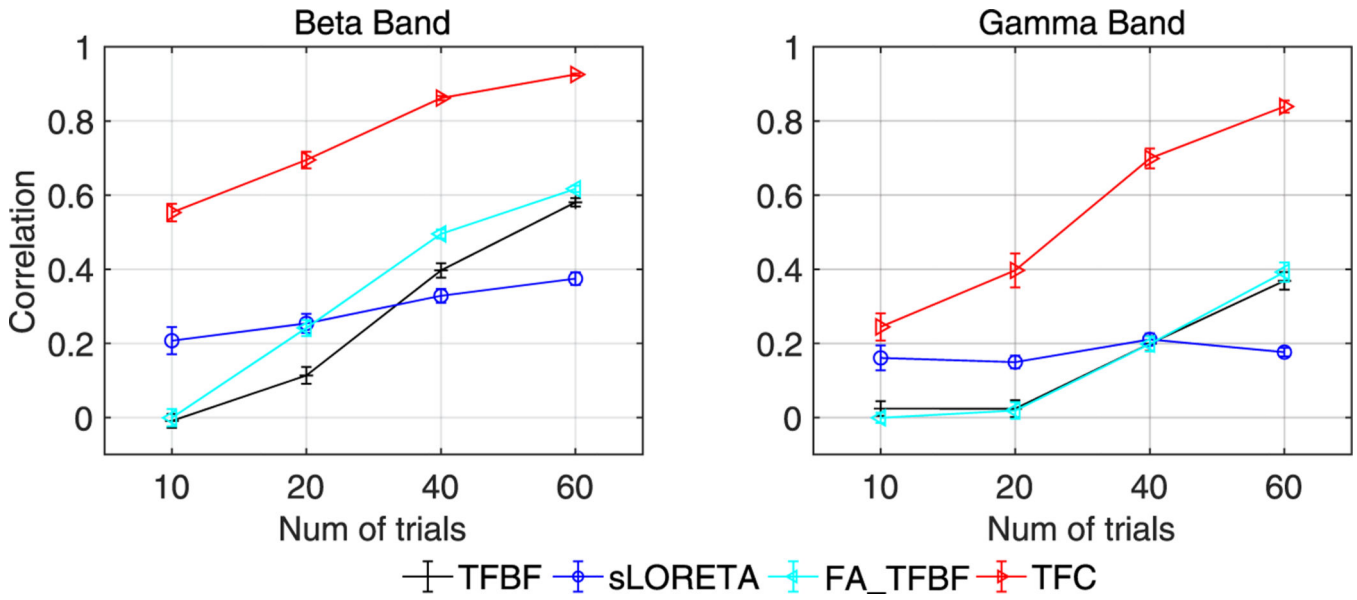

Fig. 7.

Obtained F-ratios as a function of the number of trials for left index finger movement data. Spatial correlation was calculated between the F-ratios estimated by different algorithms and the ground truth, which was defined as the F-ratio estimated from all available trials using TFC. The results were averaged across 30 simulations for each configuration. Error bars show the standard error of the mean.

Author Manuscript

Author Manuscript

Author Manuscript

Author Manuscript

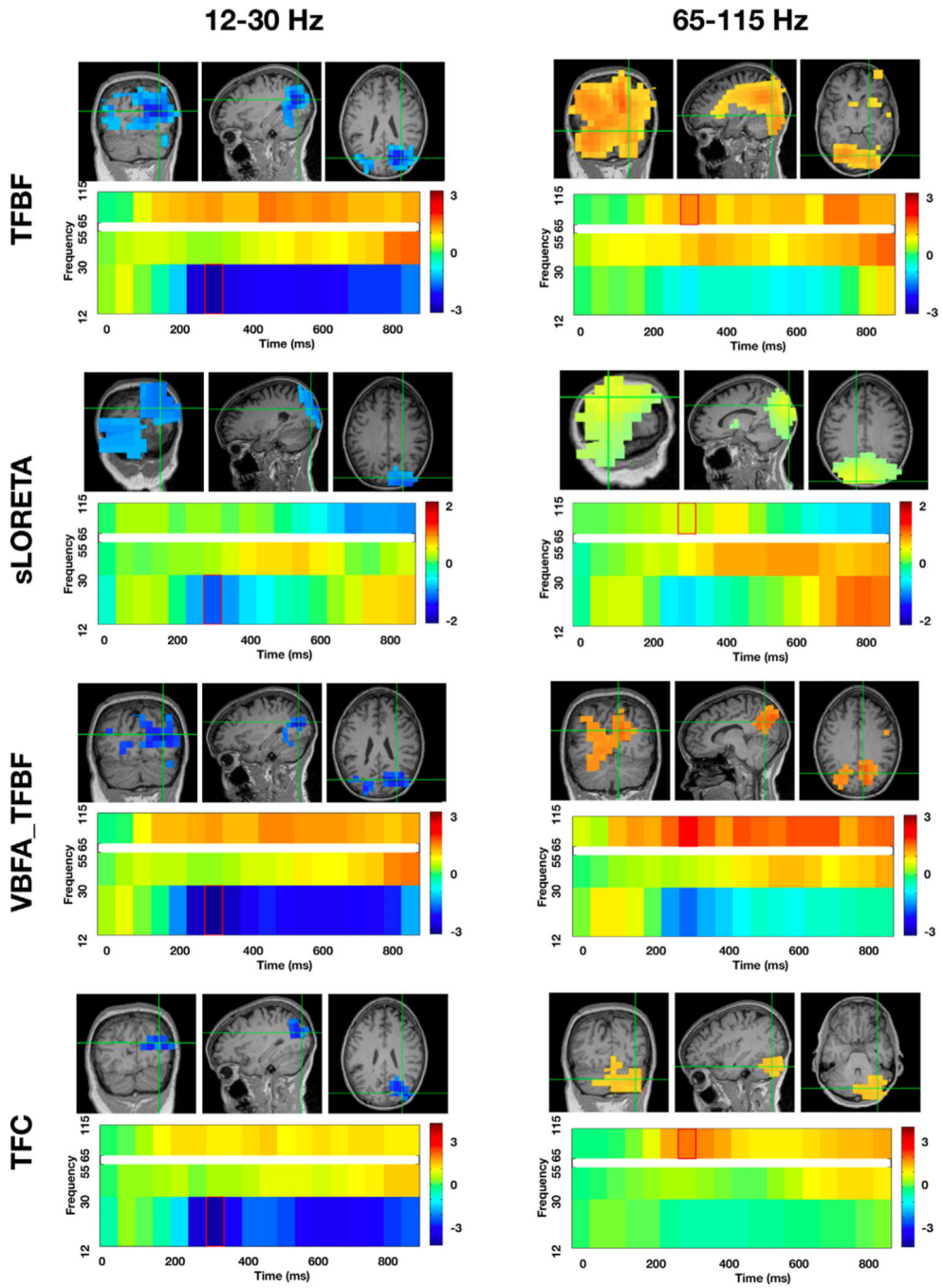

Fig. 8.

Shown above are F-ratio estimates obtained for the picture naming task using TFBF, sLORETA, VBFA_Beam and TFC. The functional maps are superimposed on each individual subject's structural MRI scan. In each of the panels, the crosshairs mark the spatiotemporal peak for the reconstructed source, with the corresponding spectrogram shown below it. The functional map plotted on the MRI corresponds to the time-frequency window highlighted in the spectrogram.

Author Manuscript Author Manuscript Author Manuscript Author Manuscript

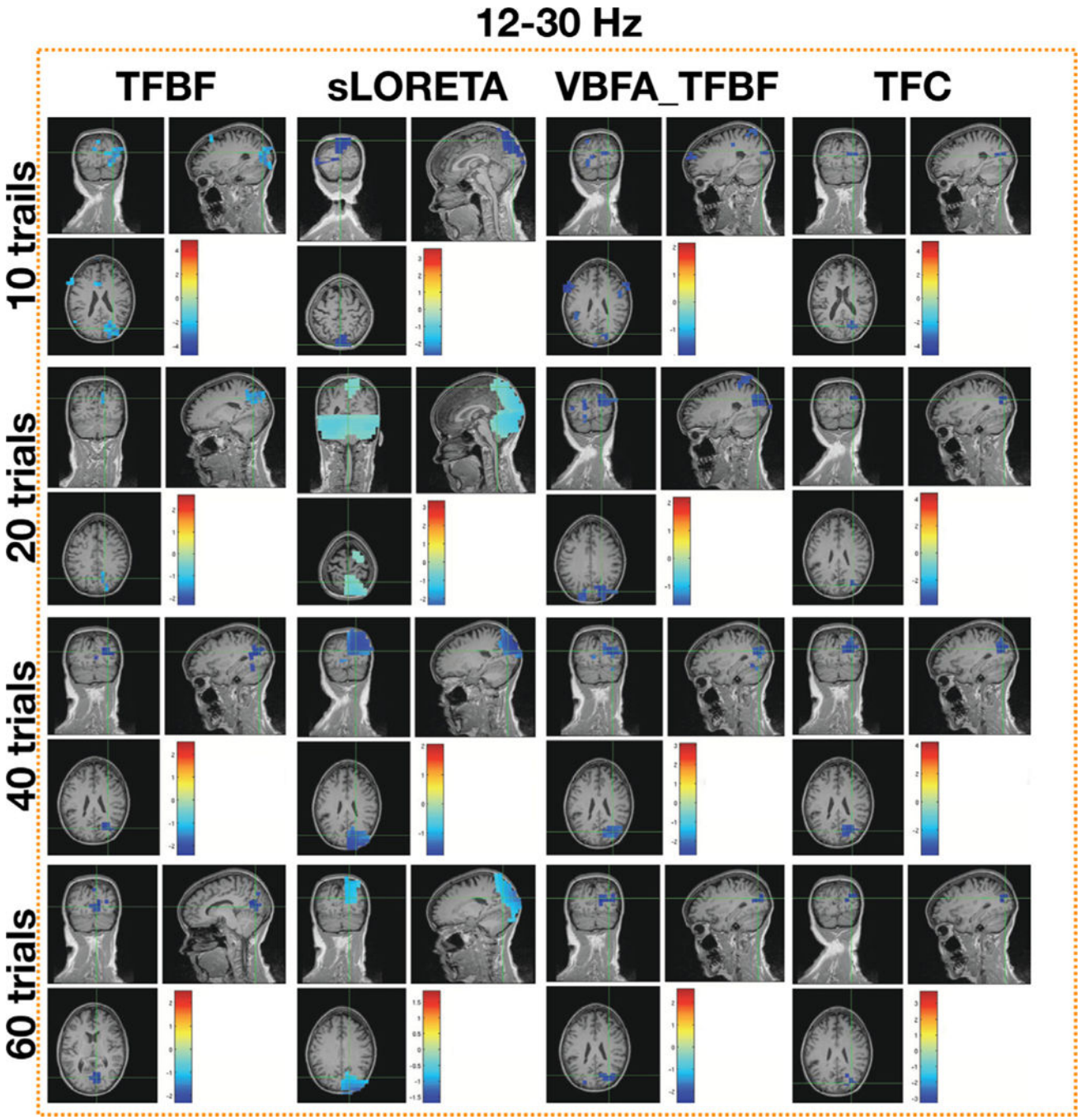

Fig. 9.

A single example showing F-ratios obtained for each algorithm on the picture naming task data in Beta band as a function of the number of trials.

Author Manuscript Author Manuscript Author Manuscript Author Manuscript

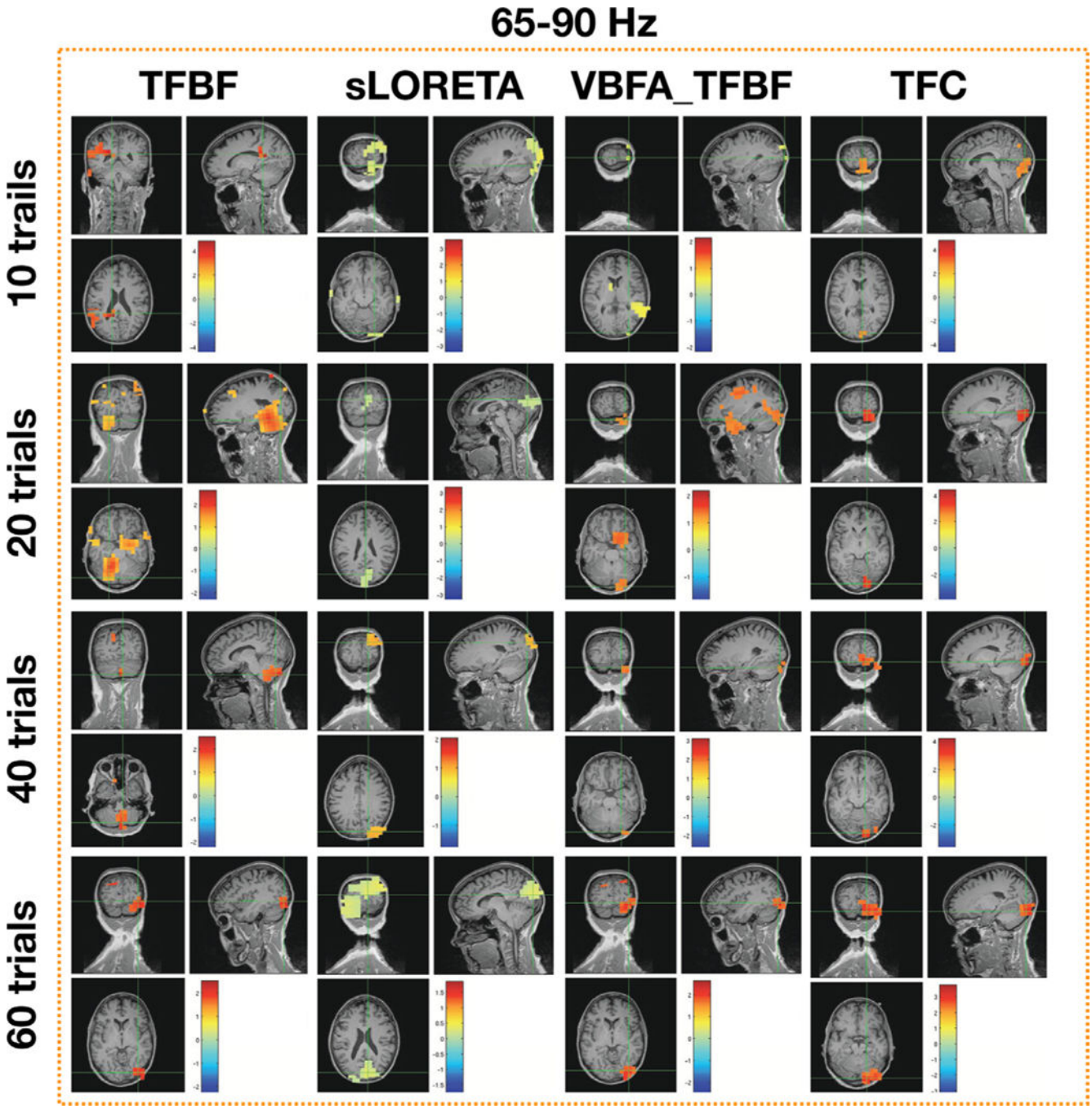

Fig. 10.

A single example showing F-ratios obtained for each algorithm on the picture naming task data in Gamma band as a function of the number of trials.

Author Manuscript Author Manuscript Author Manuscript Author Manuscript

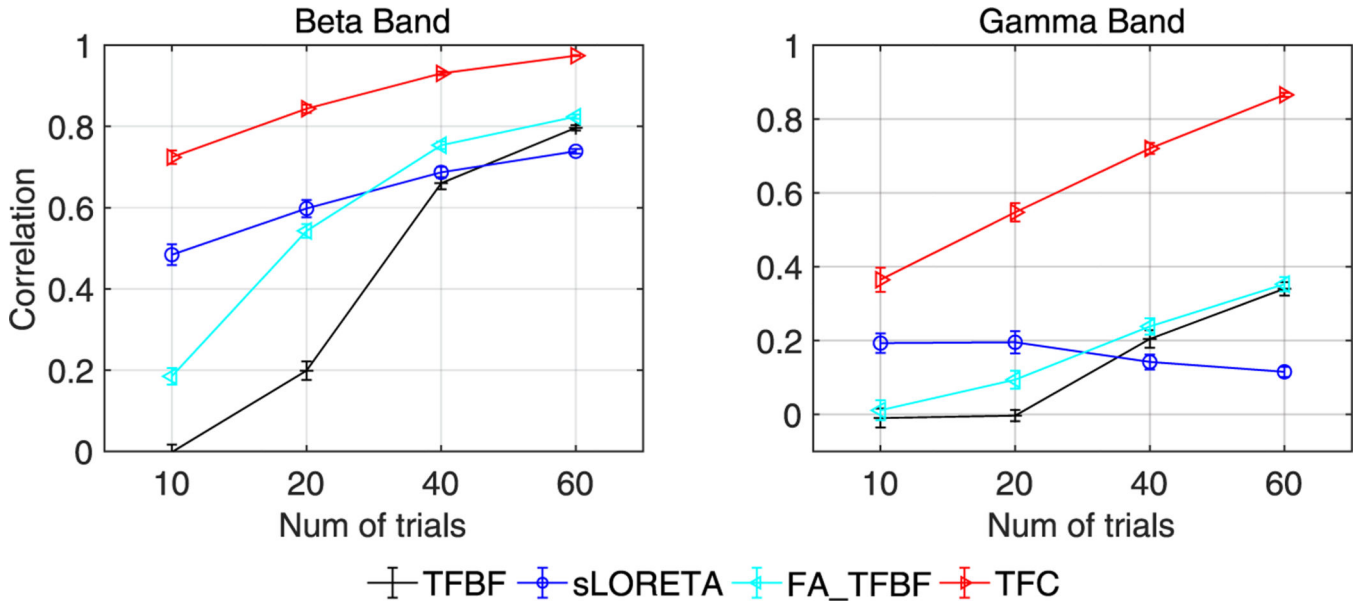

Fig. 11.

Evaluation results observed for increasing numbers of trials on the picture naming task data in the Beta and high Gamma bands. Spatial correlation was calculated between the F-ratios estimated by different algorithms and ground truth, which was defined as the F-ratio estimated by TFC using all avilable trials. The results were averaged across 30 simulations for each configuration. Error bars show the standard error of the mean.